

CHEMICALLY-INDUCED CONTROLLED GROWTH OF
CsPbBr₃ PEROVSKITE NANOCRYSTALS

A Thesis
presented to
the Faculty of the Graduate School
at the University of Missouri-Columbia

In Partial Fulfillment
of the Requirements for the Degree
Master of Science

by
MARIIA GORIACHEVA
Dr. Yangchuan Xing, Thesis Supervisor

DECEMBER 2017

The undersigned, appointed by the dean of the Graduate School, have examined the thesis entitled

CHEMICALLY-INDUCED CONTROLLED GROWTH OF
CsPbBr₃ PEROVSKITE NANOCRYSTALS

presented by Mariia Goriacheva,

a candidate for the degree of master of science,

and hereby certify that, in their opinion, it is worthy of acceptance.

Professor Yangchuan Xing

Professor Patrick Pinhero

Professor Sheila Grant

DEDICATION

I would like to dedicate this thesis to the memory of my father, Viacheslav Nikolayevich Goriachev.

ACKNOWLEDGEMENTS

I would like to express my deep appreciation to my advisor Dr. Yangchuan Xing for his valuable mentorship and continuous support. You have given me so many opportunities, and for that you have my gratitude.

I would also like to thank Dr. Sheila Grant and Dr. Patrick Pinhero for their willingness to be members of my thesis committee.

I would like to extend my thanks to Dr. Alexander Safronov and Dr. Peter Cornish, who kindly provided me with the access to their equipment. I would also like to thank Dr. Tommi White and Dr. Xiaoqing He for the prosperous collaboration.

I wish to express my appreciation to the staff of Chemical Engineering Department for providing a great learning environment.

Finally, I wish to thank all current and former students in Dr. Xing's group for their assistance with classes, and useful discussions in my research.

TABLE OF CONTENTS

ACKNOWLEDGEMENTS	ii
LIST OF ILLUSTRATIONS.....	v
Chapter I. LITERATURE REVIEW.....	1
1.1 Introduction.....	1
1.2 Synthesis of Colloidal CsPbBr ₃ Perovskite Nanocrystals.....	2
1.2.1 Hot-Injection Method.....	3
1.2.2 Room Temperature Ligand-Mediated Reprecipitation Method.....	4
1.2.3 Room Temperature Supersaturated Recrystallization Process.....	5
1.3 Size Manipulation and Shape Transformation.....	6
1.3.1 The Effect of the Injection Temperature.....	6
1.3.2 The Effect of Halogen Component.....	7
1.3.3 The Impact of Surface Ligands.....	8
1.4 Opto-Electronic Properties of Halide Perovskite Nanocrystals.....	9
1.4.1 Optical Properties.....	9
1.4.2 Electronic Properties.....	10
1.5 Applications.....	11
1.5.1 Photovoltaics.....	12
1.5.2 Light Emitting Diodes.....	13
1.5.3 Photodetectors.....	16
Chapter II. INDUCED GROWTH OF CsPbBr ₃ NANOCRYSTALS AT ROOM TEMPERATURE.....	18
2.1 Statement of the Research.....	18
2.2 Related Studies.....	18
2.2.1 Surface Chemistry of CsPbBr ₃ Nanocrystals.....	18

2.2.2 Diethylzinc as the Trigger for Nanocrystals Fusion.....	19
2.3 Experimental.....	20
2.4 Results and Discussion.....	20
Chapter III. CONCLUSIONS AND FUTURE WORK.....	30
3.1 Summary and Conclusion.....	30
3.2 Future Work.....	30
APPENDIX.....	32
BIBLIOGRAPHY.....	43

LIST OF ILLUSTRATIONS

Figure 1. CsPbBr ₃ perovskite NCs and their structural characterization. (A) Schematic of the cubic perovskite unit cell; (B) HR TEM of single CsPbBr ₃ NC; (C) TEM image of CsPbBr ₃ NCs [8].....	2
Figure 2. Schematic illustration of formation of different CsPbBr ₃ NCs by ligand-mediated re-precipitation method at room temperature. Hexanoic acid and octylamine were used for spherical quantum dots; oleic acid and dodecylamine for nanocubes; acetate acid and dodecylamine for nanorods; oleic acid and octylamine for few-unit-cell-thick nanoplatelets [9].....	4
Figure 3. Schematic illustration of formation of CsPbX ₃ NCs by supersaturated recrystallization method at room temperature. NCs were formed through transferring the Cs ⁺ , Pb ²⁺ , and X ⁻ ions from the soluble to insoluble solvents. C: ion concentration in different solvents. C ₀ : saturated solubilities in DMF, toluene, or mixed solvents (DMF+toluene) [10].....	5
Figure 4. PL spectra of samples obtained by mixing CsPbBr ₃ NCs with either CsPbCl ₃ or CsPbI ₃ [17].....	7
Figure 5. Summary of the shape and size dependence on the chain length of carboxylic acids and amines and temperature [18].....	8
Figure 6. Colloidal CsPbX ₃ NCs exhibit bright and narrow emission. (A) CsPbX ₃ NCs in toluene under UV light ($\lambda=365$ nm); (B) Normalized PL spectra for NCs displayed in A [8].....	13
Figure 7. Emission from CsPbX ₃ NCs (black data points) compared to the most common color standards: LCD TV (dashed white triangle), and NTSC TV (solid white triangle) [8].....	14
Figure 8. Illustration of multilayer perovskite-based LED device. (A) The device structure; (B) Cross-sectional TEM image of the device (scale bar is 50 nm); (C) Flat-band energy level diagram [38].....	15
Figure 9. (A) Schematic of the CsPbI ₃ -based photodetector ($L = 3$ mm, $W = 7800$ mm); (B) Photocurrent-time ($I_{ph}-t$) response measured in the dark and under illumination using a laser diode at 405 nm as a function of applied bias at a fixed light intensity ($P_{in} = 1.98$ mW cm ⁻²); (C) Rise and decay time of the photodetector device [40].....	16
Figure 10. Size evolution of CsPbBr ₃ NCs upon DEZ injection. (A) HR TEM image of as-synthesized monodisperse CsPbBr ₃ NCs, and size distribution profile; (B) immediate growth of CsPbBr ₃ upon DEZ (5 wt. %) injection. NCs have both orthorhombic and cubic shape. Insets in B: crystal lattice information of grown NCs; (C) HR TEM image of CsPbBr ₃ NCs 48 hours after DEZ injection, and size distribution profile.....	22

Figure 11. Crystallographic structure of CsPbBr ₃ NC after DEZ injection. (A) HR TEM image of CsPbBr ₃ nanocrystal; (B) Fast Fourier transform (FFT) pattern of the nanocrystal displayed in A.....	23
Figure 12. TEM images of CsPbBr ₃ NCs after injection of DEZ, and their size distribution profile: (A) CsPbBr ₃ NCs with 1 wt. % of DEZ; (B) CsPbBr ₃ NCs with 5 wt. % of DEZ.....	24
Figure 13. Energy Dispersive Spectroscopy of grown NCs. (A) HR TEM image of a region with grown CsPbBr ₃ NCs; (B) Elemental mapping for Zn for a region displayed in (A); (C) Artificially enhanced image of B (red squares represent Zn).....	26
Figure 14. Optical properties of grown NCs. (A) UV-vis absorption and (B) PL emission spectra for CsPbBr ₃ before (blue) and after (red) DEZ injection.....	27
Figure 15. Thickness of grown NCs. (A) Electron Tomography image of CsPbBr ₃ NCs after 5 wt. % DEZ injection; (B) Thickness profile of NC displayed in A.....	28
Scheme 1. Proposed reaction path of DEZ with carboxylates on the surface of CsPbBr ₃ NCs. Upon dissociation, DEZ reacts with carboxylate anion forming C ₂ H ₅ -Zn-OOR compound. Oleylammonium donates hydrogen atom to the remaining ethyl group to produce ethane.....	25

Chapter I. LITERATURE REVIEW

1.1 Introduction

Trihalide perovskite nanocrystals (NCs) have recently emerged as a new class of superior nanoscale semiconductors. Perovskite NCs with AMX_3 formula (where A is an organic or inorganic cation, M is a bivalent metal (typically Pb or Sn), and X is a halogen (I, Br, or Cl)) can be divided into two families with respect to the nature of cation A: 1) hybrid organic-inorganic perovskite NCs (with an organic cation, e.g. CH_3NH_3), and 2) all-inorganic perovskite NCs (with an inorganic cation, e.g. Cs). Miyasaka and collaborators first introduced hybrid organic-inorganic perovskite NCs into photovoltaic cells as visible-light sensitizers in 2009 [1]. At that time, the study did not attract broad attention mainly due to a relatively low photovoltaic efficiency (3.8%) and a significant degradation of solar cells upon continuous irradiation. Yet, a tremendously extensive research was generated by two independent groups in 2012, when the liquid electrolyte was replaced with a solid hole-transport layer [2, 3]. According to the latest achievements, the power conversion efficiency of hybrid perovskite-based solar cells have already exceeded 20%, which is on par with the best light adsorbing material up to date – silicon [4-6]. However, poor long-term stability of hybrid perovskite solar cells, due to a volatile nature of the organic cation, remains the biggest challenge to overcome. In this regard, a family of all-inorganic perovskite NCs ($CsPbX_3$, where X=I, Br, or Cl) is rapidly gaining researchers' attention due to its superior resistance to moisture, elevated temperatures, and long irradiation [7]. $CsPbBr_3$ have become the most studied NCs in its family, largely due to a combination of their long lifetime and a reasonably appropriate for photovoltaics band gap.

1.2 Synthesis of CsPbBr₃ Perovskite Nanocrystals

Colloidal CsPbBr₃ perovskite NCs were first successfully synthesized by Protesescu *et al.* by hot-injection method in 2015 [8]. The synthesis yielded cubic shaped perovskite NCs with a remarkably narrow size distribution (Figure 1).

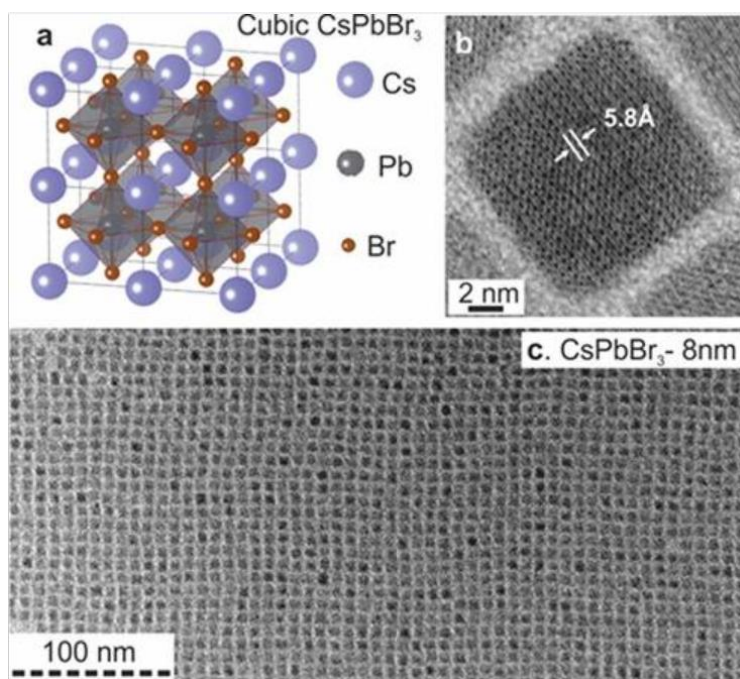


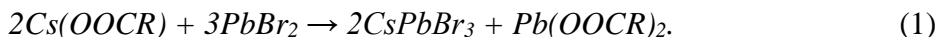
Figure 1. CsPbBr₃ perovskite NCs and their structural characterization. (A) Schematic of the cubic perovskite unit cell; (B)HR TEM of single CsPbBr₃ NC; (C) TEM image of CsPbBr₃ NCs [8].

Relatively high temperatures (140-200°C) as well as the inert atmosphere were required in hot-injection method. Consequently, researchers focused on developing chemical routes allowing the production of perovskite NCs in ambient atmosphere at room temperature. This resulted in the development of two additional methods: room temperature ligand-mediated reprecipitation method by Sun *et al.*, and room temperature supersaturated recrystallization process by Li *et al.* [9, 10]. The comparative description of

these three methods will be discussed later. Though, it was shown that CsPbBr₃ NCs could be also synthesized by chemical vapor deposition (by epitaxial growth on the substrate); the method did not receive much attention mostly due to the engineering complexity of the procedure [11, 12].

1.2.1 Hot-Injection Method

The synthesis of CsPbBr₃ NCs by hot-injection method was accomplished by the injection of Cs-oleate into octadecene solution containing lead bromide (PbBr₂), oleylamine, and oleic acid. The injection was typically performed at elevated temperatures (140-200°C) under nitrogen atmosphere. Oleylamine and oleic acid served as stabilizing surfactants in colloidal dispersion. Of note, the addition of both was essential, as PbBr₂ could only be dissolved in the presence of both ligands. The mechanism of reactions taking place in hot-injection method was heavily investigated by De Roo *et al.* [13]. According to their findings, PbBr₂ reacted with oleic acid, prior to Cs-oleate injection, through anion exchange. The reaction resulted in the formation of lead oleate and oleylammonium bromide, which also served as stabilizing surfactants after CsPbBr₃ NCs were formed. Therefore, the procedure of NCs formation by hot-injection method can be described as following:



Despite the high crystalline quality of as-synthesized NCs and their substantially narrow size distribution, the method could not be elevated to a gram-scale production. Still, the procedure developed by Protesescu and collaborators is the most widely adopted among researchers.

1.2.2 Room Temperature Ligand-Mediated Reprecipitation Method

In ligand-mediated reprecipitation method, the precursors are usually dissolved in a ‘good’ solvent (e.g. such polar solvents as dimethylformamide, tetrahydrofuran, dimethyl sulfoxide), and then are mixed with a ‘bad’ solvent (mainly non-polar solvents; e.g. toluene, hexane, etc.) [9]. Upon mixing with the ‘bad’ solvent, CsPbBr₃ NCs form. The authors suggested that the formation of the NCs happened due to a co-precipitation of Cs⁺, Pb²⁺, and Br⁻ ions in the presence of stabilizing surfactants. Following this procedure, CsPbBr₃ NCs of various shapes were successfully synthesized: spherical quantum dots, nanocubes, one-dimensional nanorods, and two-dimensional nanoplatelets (Figure 2) [9].

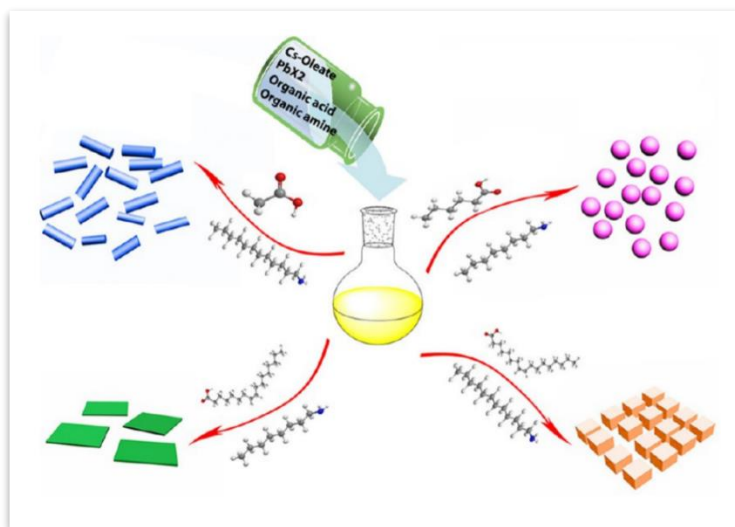


Figure 2. Schematic illustrating formation of different CsPbBr₃ NCs by ligand-mediated re-precipitation method at room temperature. Hexanoic acid and octylamine were used for spherical quantum dots; oleic acid and dodecylamine for nanocubes; acetate acid and dodecylamine for nanorods; oleic acid and octylamine for few-unit-cell-thick nanoplatelets [9].

One of the advantages of the reprecipitation method is that the procedure is carried out in open air at room temperature. So, the synthesis could be extended to a gram-scale level by scaling up the precursors. Unfortunately, it has been shown that the use of polar solvents can also degrade the as-synthesized NCs, resulting in a lower yield. Given this concern, Wei *et al.* developed a novel chemical route utilizing non-polar solvent only (toluene). The procedure was performed at room temperature in the ambient atmosphere enabling gram-scale synthesis of CsPbBr₃ NCs [14].

1.2.3 Room Temperature Supersaturated Recrystallization Process

Supersaturated recrystallization is a method based on mixing the solvents with different polarities. Li *et al.* were among the first who successfully synthesized CsPbBr₃ NCs by recrystallization method (Figure 3) [10].

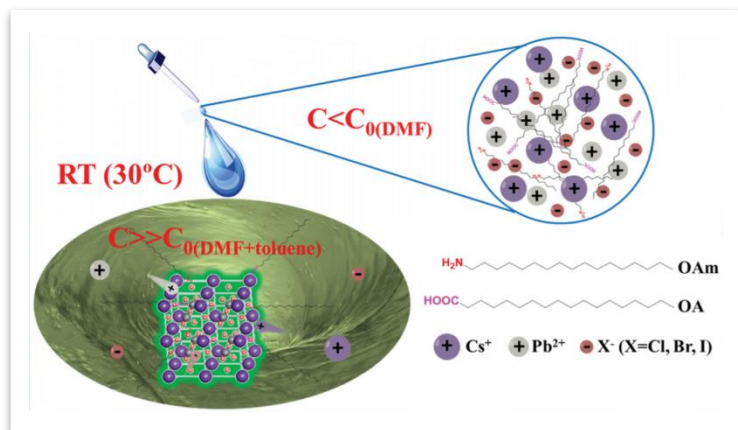
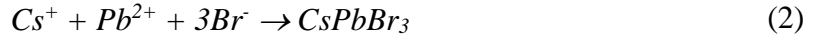


Figure 3. Schematic illustrating formation of CsPbX₃ NCs by supersaturated recrystallization method at room temperature. NCs were formed through transferring the Cs⁺, Pb²⁺, and X⁻ ions from the soluble to insoluble solvents. C: ion concentration in different solvents. C₀: saturated solubilities in DMF, toluene, or mixed solvents (DMF+toluene) [10].

The synthesis was carried out through transferring Cs^+ , Pb^{2+} , and Br^- ions from soluble solvent to insoluble solvent. Such a transfer created a supersaturated state, which allowed formation of CsPbBr_3 perovskite NCs in the presence of organic stabilizing surfactants. Again, the procedure was conducted in open air at room temperature, allowing gram-scale production. The overall procedure can be described by the following equation:



1.3 Size Manipulation and Shape Transformation of CsPbBr_3 Perovskite Nanocrystals

It was found that the size of CsPbBr_3 NCs as well as their shape could be altered. This was accomplished by modifying different parameters, including: temperature of the injection, halogen component, and stabilizing surfactants. The impacts of these factors are described in detail below.

1.3.1 The Effect of the Injection Temperature

In the original synthesis procedure by hot-injection method, the authors discovered the following size-temperature dependence: the higher the temperature of injection the bigger the size of as-synthesized NCs [8]. Varying the injection temperature from 140°C to 200°C yielded cubic shaped NC with *approx.* average sizes of 4 and 15 nm, respectively. The size of perovskite NCs also had a direct impact on its band gap, known as quantum confinement effect: the bigger the nanocrystal, the smaller the band gap. Later, Bekenstein *et. al.* showed that lowering the temperature of injection to 90°C-130°C produced two-dimensional (2D) nanoplatelets (NPLs) with a minimum thickness of a single unit cell [15].

Although it was shown that lower temperatures of injection favored the formation of 2D NPLs, rather than NCs, the cause is still not well understood. Further attempts in developing the synthesis of CsPbBr₃ NCs of different shapes were focused on eliminating the need for elevated temperatures and inert atmosphere (the aforementioned supersaturated recrystallization and reprecipitation method). As a result, CsPbBr₃ NCs of different shapes including spherical quantum dots, nanocubes, one-dimensional nanorods, and 2D NPLs were successfully synthesized at room temperature [9, 16].

1.3.2 The Effect of Halogen Component

While temperature of injection had the most impact on the size of NCs (with only mild changes in their band gaps), a direct anion-exchange reaction was found to be the most effective way for band gap alterations [17].

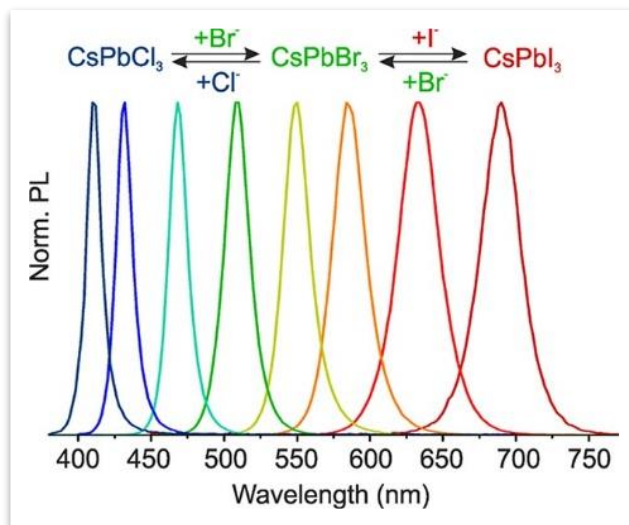


Figure 4. PL spectra of samples obtained by mixing CsPbBr₃ NCs with either CsPbCl₃ or CsPbI₃ [17].

It has been found that the as-synthesized tri-halide perovskite NCs can readily participate in anion-exchange reactions, which allowed tuning of the band gap over the

entire visible region. Upon mixing as-synthesized tri-halide NCs with certain ratio of desired halide source, the authors were able to obtain uniform mixed halide perovskites, including $\text{CsPb}(\text{Br}/\text{I})_3$ and $\text{CsPb}(\text{Br}/\text{Cl})_3$ (Figure 4). Interestingly, anion-exchange reactions did not alter the original size of NCs. This could be explained by the existence of inner layer of stabilizing surfactants on the surface of NC, which protects them from agglomeration in anion-exchange process.

1.3.3 The Impact of Stabilizing Surfactants

An extensive research on the role of stabilizing surfactants in determining the size and shape of future CsPbBr_3 NCs was conducted by Pan *et. al.* [18].

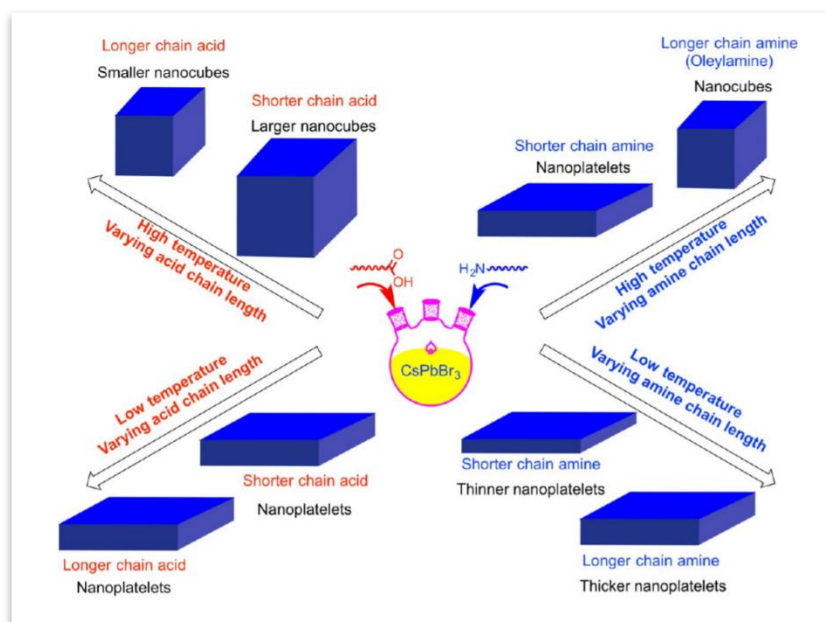


Figure 5. Summary of the shape and size dependence on the chain length of carboxylic acids and amines and temperature [18].

The authors discovered that in addition to the temperature effect, the choice of stabilizing surfactants had a significant impact on the CsPbBr_3 NCs shape and size. By

varying the chain length of stabilizing surfactants – carboxylic acids and amines – the author made the following conclusions: 1) oleylamine paired with carboxylic acids, with shorter chain length (versus oleic acid), produced bigger nanocubes; 2) oleic acid paired with amines with shorter chain lengths (versus oleylamine), produced nanoplatelets with a thickness varying with the amines' length. The shortest amines produced the thinnest nanoplatelets.

1.4 Opto-Electronic Properties of Tri-Halide Perovskite Nanocrystals

An extensive interest toward tri-halide perovskite NCs was driven primarily due to their exceptional opto-electronic properties. Perovskite NCs exhibit several superior properties: strong optical absorption, widely tunable band gap, remarkable photoluminescence, large charge carrier mobility, exceptional electron-hole diffusion length, and a unique defect-tolerant photophysics. The existing knowledge on optical and electronic properties is summarized in this chapter.

1.4.1 Optical Properties

Tri-halide perovskite NCs display exceptionally strong optical absorption. For example, the optical absorption coefficient of $\text{CH}_3\text{NH}_3\text{PbI}_3$ (within the visible light range) is up to 1 order of magnitude higher than that of GaAs - the absorber with the highest efficiency among thin film solar cells [19]. Since visible light accounts for the major portion of usable light, the large optical absorption coefficient plays an essential role in highly efficient solar cells. According to Yin *et al.* high optical coefficients in halide perovskites originate from combination of perovskite symmetry, p - p orbital transitions, and

a direct band gap. The authors theorized that the unoccupied Sn/Pb p orbitals contribute to the lower parts of the conduction bands in halide perovskites, whereas the upper valence bands mostly consist of halogen p orbitals and a small amount of Sn/Pb s orbitals. Thus, full occupation of s orbitals below valence band maximum allows p - p transitions occur [19]. The realization of p - p transitions, in addition to a direct band gap in halide perovskites, results in their superior optical absorption of visible light. As aforementioned, the band gap of halide perovskites could be easily tuned over the entire visible region [8, 17].

In addition to enhanced optical absorption, halide perovskites exhibit remarkably bright photoluminescence with narrow emission lines widths (12-42 nm), and a quantum yield reaching up to 90% for CsPbI₃ NCs [8]. Of note, a similar result was achieved for CdSe quantum dots, but only when passivating them with CdS shell [56-57]. In contrast to uncoated quantum dots, stabilizing ligands on the surface of NCs do not impart significant midgap trap sites [8].

1.4.2 Electronic Properties

In addition to exceptional optical properties, tri-halide perovskite NCs exhibit extraordinary carrier transport properties, including: high mobility, long relaxation time, and remarkable diffusion length. As an example, the mobility life time product ($\mu\tau$) for electrons and holes in CsPbBr₃ were estimated to be $1.7 \times 10^{-3} \text{cm}^2/\text{V}$ and $1.3 \times 10^{-3} \text{cm}^2/\text{V}$, respectively [20]. The remarkably high values of $\mu\tau$ imply high mobility and high relaxation time in CsPbBr₃. As such, the mobility of electrons was estimated to be

$\sim 1000 \text{ cm}^2/(\text{V} \cdot \text{s})$, which is on par with Si. Relaxation time was found to be of the order of a few microseconds [20, 21].

High mobility in tri-halide perovskite NCs is usually accompanied with an exceptionally large carrier diffusion length. It was found that the electron-hole diffusion length in mixed tri-halide perovskites exceeded 1 micrometer, being ~ 5 to 10 times greater than the absorption depth [22]. The diffusion length in $\text{CH}_3\text{NH}_3\text{PbI}_3$ was estimated to be at least 100 nm, which was still comparable to the absorption depth of the material [22, 23]. Longer diffusion length in relation to absorption depth is the key factor in obtaining high photovoltaic efficiency.

In an attempt to understand the cause for exceptional carrier transport properties in tri-halide perovskites, scientists turned their attention toward atomistic origins of perovskite NCs. It was found that the native point defects (including vacancies, interstitials, and antisites) mostly create shallow levels in the band gap, meaning they are insignificant in terms of carrier trapping [19, 24]. The lack of carrier traps along with p - p orbital transitions, small effective masses, and a direct band gap results in exceptional optoelectronic properties of halide perovskites.

1.5 Applications

Given the outstanding tunable optoelectronic properties, halide perovskites exhibit a great potential in a variety of applications, including photovoltaic devices, light emitting diodes, and photodetectors. In this section, we will address current state of inorganic perovskites with regard to these applications.

1.5.1 Photovoltaics

The field of photovoltaics was revolutionized with the emergence of organic-inorganic perovskite NCs. Hybrid perovskites quickly proved to be one of the most promising light absorbing materials [25-27]. The combination of properties such as strong optical absorption, widely tunable band gap, long diffusion length, and defect-tolerant photophysics resulted in a rapid development of highly efficient perovskite-based solar cells. According to the most recent achievements, the highest certified power conversion efficiency has already reached 22.1% [28]. Initially, the accomplishment of highly efficient performance of perovskite-based solar cells was related to the organic cation in hybrid perovskites. In 2015, Kulbak *et al.* proved that replacing the organic cation with inorganic Cs not only allowed reaching high open circuit voltage (V_{oc}), but also significantly increased solar cell resistance to the elevated temperatures [7]. Later, a few groups showed that adding inorganic Cs to the organic cation also led to increased stability [29-31]. Eperon *et al.* were the first to introduce all-inorganic CsPbI₃-based perovskite solar cell, further solidifying that the substitution of volatile organic cation with inorganic led to a significant improvement of thermal stability of the cell without any loss in efficiency [32]. Despite having the most suitable band gap (~1.6 eV) among all-inorganic perovskites, CsPbI₃ NCs rapidly degrade at room temperature, transforming from perovskite α -phase into non-perovskite δ -phase, subsequently losing its unique optoelectronic properties [32]. Fittingly, further work was focused on preserving CsPbI₃ perovskite α -phase [32-34]. The efficiency of the most recent α -phase CsPbI₃ perovskite solar cell was estimated to be 10.77% [34]. Meanwhile, extensive research on employing CsPbBr₃ perovskites also produced significant results. Two independent groups pioneered CsPbBr₃-based solar cells with hole

transport layer and cathode, both made of carbon pasta [35, 36]. The devices demonstrated the efficiencies of 5.0% and 6.7%, respectively in addition to an exceptional stability in high humidity and extreme temperatures without any additional encapsulation [35, 36].

1.5.2 Light Emitting Diodes

Another fast developing field in the application of inorganic perovskite NC is light emitting diodes (LEDs). Perovskites exhibit few essential properties for efficient light emitting devices, including bright photoluminescence (PL) with narrow emission lines, high PL quantum yield (reaching up to 90%), and a tunable emission over the entire visible region (Figure 6) [8].

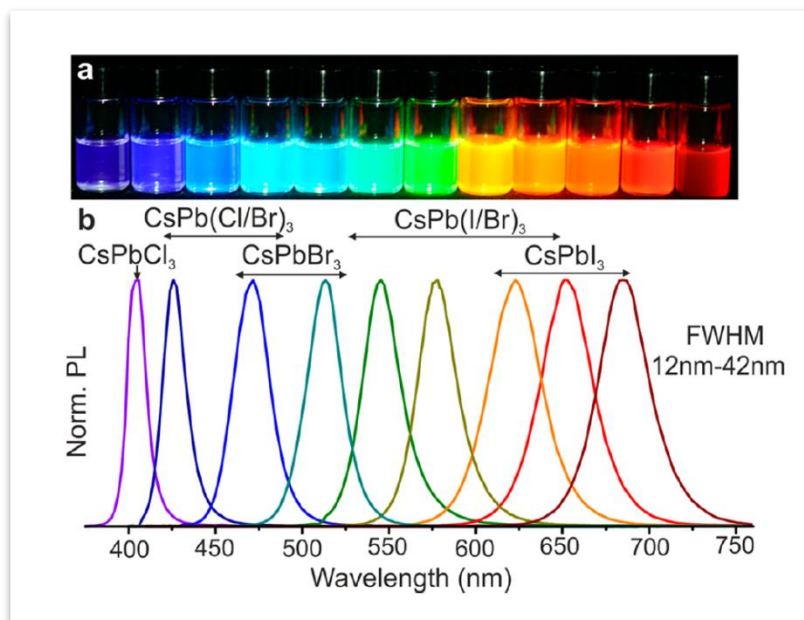


Figure 6. Colloidal CsPbX₃ NCs exhibit bright and narrow emission. (A) CsPbX₃ NCs in toluene under UV light ($\lambda=365$ nm); (B) Normalized PL spectra for NCs displayed in A [8].

It was shown that organic CsPbX₃ NC emission covers 140% of the National Television System Committee (NTSC) standard (Figure 7), whereas CdSe-based quantum dot emission executes less than 100% [8, 37].

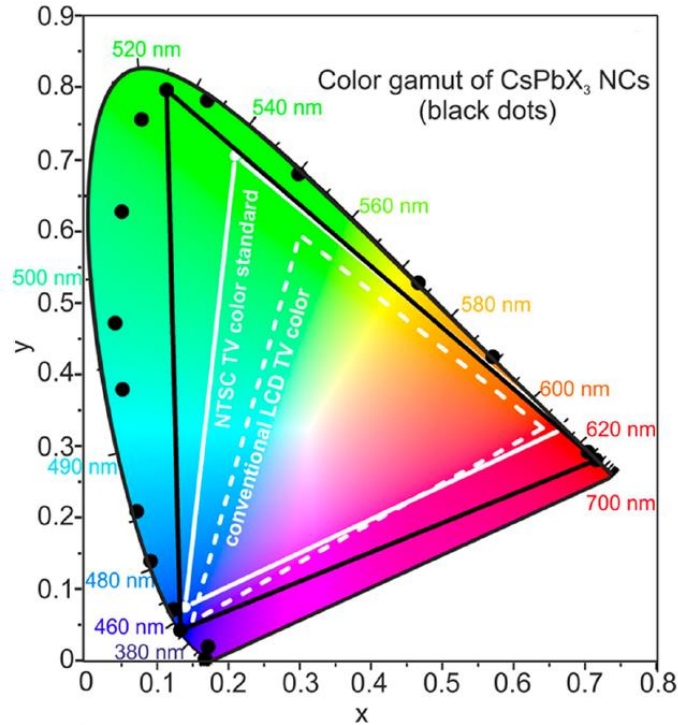


Figure 7. Emission from CsPbX₃ NCs (black data points) compared to the most common color standards: LCD TV (dashed white triangle), and NTSC TV (solid white triangle) [8].

In 2015, Song and collaborators pioneered the first inorganic perovskite-based LEDs [38]. The devices consisted of the following layers: indium tin oxide (ITO), poly(ethylenedioxythiophene):polystyrene sulfonate (PEDOT:PSS, 40 nm), poly(9-vinylcarbazole) (PVK, 10 nm), perovskite NCs (10 nm), TPBi (40 nm), and LiF/Al (1/100 nm). PVK served as a hole transporting layer and TPBi as an electron transporting layer (Figure 8) [38]. Electrons were injected into perovskite layer where they radiatively recombined, emitting light. The luminances of 742 cd m⁻², 946 cd m⁻², and 528 cd m⁻²

with external quantum efficiencies (EQE) of 0.07%, 0.12%, and 0.09% were achieved for blue, green and orange LEDs, respectively [38].

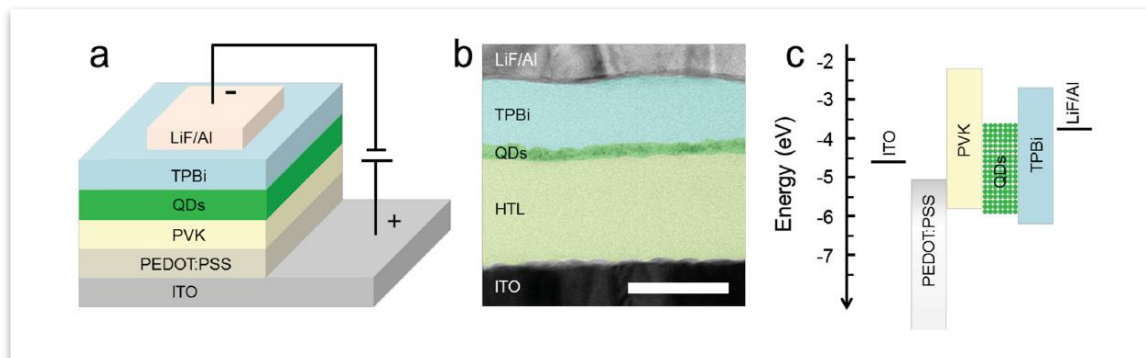


Figure 8. Illustration of multilayer perovskite-based LED device. (A) The device structure; (B) Cross-sectional TEM image of the device (scale bar is 50 nm); (C) Flat-band energy level diagram [38].

The small EQE remains the biggest challenge in the development of perovskite-based LEDs. To some extent, the low performance was explained by the existence of a relatively insulating layer of organic ligands (oleic acid, oleylamine) present on the surface of nanocrystals. Pan and collaborators attempted to increase the EQE of inorganic perovskite-based LEDs by substituting long-chain ligands with short didodecyldimethylammonium bromide through ligand exchange [39]. The maximum EQE and luminance of 3.0% and 330 cd m^{-2} was achieved for green LEDs. The authors proved that didodecyldimethylammonium bromide offered better surface passivation, resulting in a better charge carrier balance and higher EQE of the device. This study undeniably demonstrated the importance of stabilizing ligands on the surfaces of NCs.

1.5.3 Photodetectors

A photodetector is a device that receives the light signal, and instantly converts it into an electric one. Semiconductors are considered to be the best material choice for energy detection due to the band gap, which serves as the energetic barrier, filtering out noise signals (which simply come from the undesired thermal carrier ‘hopping’). Given the exceptional electronic properties, solution-processed inorganic perovskite nanocrystals seem to be very promising candidates for photodetectors. In 2016, Ramasamy *et al.* introduced photodetector devices based on all-inorganic CsPbI₃ NCs for the first time [40]. The devices consisted of a thin perovskite film, drop-casted on a heavily doped Si substrate and pre-patterned gold electrodes. An exceedingly good photosensitivity, which is defined as the on/off photocurrent ratio, was achieved (10^5). The rise and decay times were estimated to be 24 and 29 ms, respectively (Figure 9) [40].

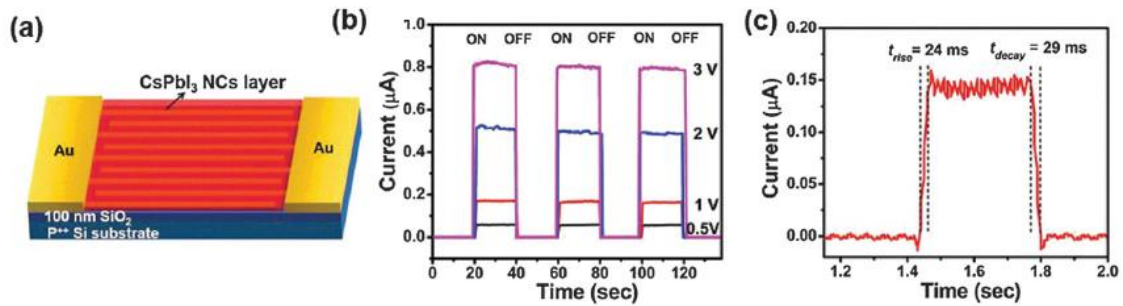


Figure 9. (A) Schematic of the CsPbI₃-based photodetector ($L = 3 \text{ mm}$, $W = 7800 \text{ nm}$); (B) Photocurrent-time ($I_{ph}-t$) response measured in the dark and under illumination using a laser diode at 405 nm as a function of applied bias at a fixed light intensity ($P_{in} = 1.98 \text{ mW cm}^{-2}$); (C) Rise and decay time of the photodetector device [40].

Later, Song *et al.* established ultrathin flexible photodetectors based on 2D CsPbBr₃ NPLs [41]. The devices demonstrated a high stability along with outstanding flexibility (>10 000 cycles). Of note, the rise and decay times were estimated to only be 19 and 25 μ s, which was considerably smaller than that for CsPbI₃-based devices. Authors concluded that the faster response time for CsPbBr₃ NPLs was due to their 2D structure, which in their opinion is more favorable for carrier transport.

Chapter II. INDUCED GROWTH OF CsPbBr₃ PEROVSKITE NANOCRYSTALS AT ROOM TEMPERATURE

2.1 Statement of the Research

Recently a few groups reported the unique ability of 2D CsPbX₃ NPLs to undergo spontaneous post-synthetic growth at room temperature by self-oriented face-to-face stacking into complex structures [42, 18]. Udayabhaskararao *et. al.* discovered that the growth of NPLs via crystallographic orientation could be triggered by the addition of polar solvents (acetone, ethanol) [43]. The authors believed that the origin of such crystallographic oriented attachment of NPLs was related to the loss of stabilizing ligands from their surfaces. In the effort to determine the impact of forced detachment of stabilizing ligands from the surface of NC, we developed a novel route, allowing induced growth of CsPbBr₃ NCs at room temperatures. An exothermic chemical reaction, taking place on the surface of NCs, lead to an impulsive removal of highly dynamic surfactants and a subsequent fusion of the NCs. The performed technique showed that highly dynamic passivating ligands on the surface of perovskites not only served for preserving colloidal dispersion, but also could be successfully used for post-synthetic manipulation of the NC size.

2.2 Related Studies

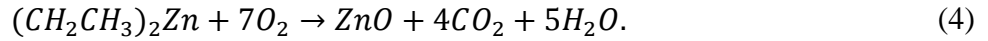
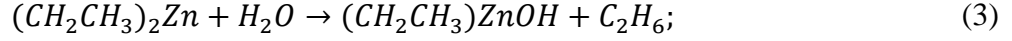
2.2.1 Surface Chemistry of CsPbBr₃ Nanocrystals

In developing our experiment, we focused our attention on the types of ligands present on the NC surfaces. Three independent groups conducted research on the nature of

these surfactants. Initially, Kim *et al.* found that surfaces of NCs were passivated with carboxylates only [44]. In contradiction, De Roo *et al.* stated that CsPbBr₃ NCs were dynamically stabilized by either oleylammonium bromide or oleylammonium oleate [45]. They also proposed that oleic acid itself did not bind to the NC surface, but rather oleic acid protonated oleylamine yielding oleylammonium carboxylate. Later, Pan *et al.* discovered that both alkylammonium and carboxylate ligands were present on the surface [18]. Additionally, the authors discovered that the carboxylate ligand, in comparison to alkylammonium, was more resistant to detachment during NCs purification with polar solvents. With respect to the existing information, we made two assumptions: 1) carboxylate is present on the surface, whether as an ion pair with oleylammonium or in a free ionic form; and 2) it is more resistant to forced detachment. We therefore chose the carboxylate anion as the target for the surface reaction.

2.2.2 Diethylzinc as the Trigger for Nanocrystals Fusion

Diethylzinc (DEZ) was selected as a precursor for a surface reaction with carboxylate anions. The choice of DEZ as a reactant followed from its well-known high reactivity with water and oxygen. DEZ has been used extensively as a precursor for producing highly oriented zinc oxide (ZnO) films, via metalorganic chemical vapor deposition [46-50]. Within this process, DEZ undergoes exothermic dissociation with a formation of Zn-O bond; and a release of ethane (in reaction with water) or oxygen and water (in reaction with oxygen) [51-54]. The ideal mechanisms of these reactions could be described with the following equations:



We implemented this knowledge in our experiments.

2.3 Experimental

Materials and chemicals. Lead bromide (PbBr₂, Aldrich, 99.999%), 1-octadecene (ODE, Aldrich, 90%), oleic acid (OA, Sigma-Aldrich, 90%), oleylamine (OLA, Aldrich, 70%), cesium carbonate (Cs₂CO₃, Aldrich, 99%), diethylzinc (DEZ, Aldrich, ≥52 wt. % Zn basis), n-heptane (anhydrous, Sigma-Aldrich, 99%), acetone (Sigma-Aldrich, ≥99.9%).

Synthesis of Cs-oleate. Cs₂CO₃ (0.407g) was loaded into a 50 ml 3-neck flask along with ODE (20 ml) and OA (1.25 ml); dried up in vacuum for 1 hour at 120°C. The solution was then heated up to 150°C under N₂ atmosphere until all Cs₂CO₃ has reacted with OA. Note that the solution must be preheated to 100°C before the injection.

Synthesis of CsPbBr₃ NCs. PbBr₂ (0.0069 g) was loaded into a 25 ml 3-neck flask along with ODE (5 ml) and dried up in vacuum for 1 hour at 120°C. OA (0.5 ml) and OLA (0.5 ml) were injected at 120°C under N₂ atmosphere. After complete solubilisation of PbBr₂, the mixture was heated up to 180°C and Cs-oleate (0.4 ml) was injected. Upon ~10 sec, the mixture was cooled down with the water-ice bath. The synthesis yielded cubic-shaped NCs with an average size of 8 nm.

Purification and Isolation of NCs. Acetone (6 ml) was added to as-synthesized NCs, and the mixture was centrifuged at 4000 rpm for 10 minutes. The supernatant was decanted, and the NCs were redispersed in n-heptane anhydrous (6 ml). Hereafter this product is referred to the ‘as-synthesized’ NCs.

Diethylzinc Induced Growth of CsPbBr₃ NCs. 0.2M solution of DEZ in n-heptane anhydrous was injected to as-synthesized CsPbBr₃ NCs in the glovebox under Ar atmosphere at room temperature. The concentration of DEZ added to NCs was calculated in regards to the mass of NCs present in the solution. 5 wt. % of DEZ was experimentally found to produce the best results in terms of growth and size distribution. Upon DEZ injection, the NC solution was stirred for 1 min in the glovebox, and then it was diluted with n-heptane anhydrous in [1:10] ratio in ambient air for further analysis. Hereafter referred to the ‘grown’ NCs.

NC Characterization Methods. UV-Vis absorption spectra were collected with Agilent Cary 60 UV-Vis Spectrophotometer. Photoluminescence (PL) spectra were obtained with Varian Cary Eclipse fluorescence spectrometer. Transmission Electron Microscopy, Energy Dispersive X-Ray Spectroscopy, and Electron Tomography were all performed on FEI Tecnai F30 Twin 300kV transmission electron microscope. 3D Model of grown NCs was constructed with the help of IMOD 4.9 and Amira 5.3 software.

2.4 Results and Discussion

The growth of NCs was documented with the transmission electron microscope (TEM) within 48 hours after DEZ injection. It was found that growth of NC occurred immediately after DEZ injection, resulting in NC size evolution from 8 to 59 nm in lateral dimensions, displaying both cubic and rectangular shapes (Figure 10).

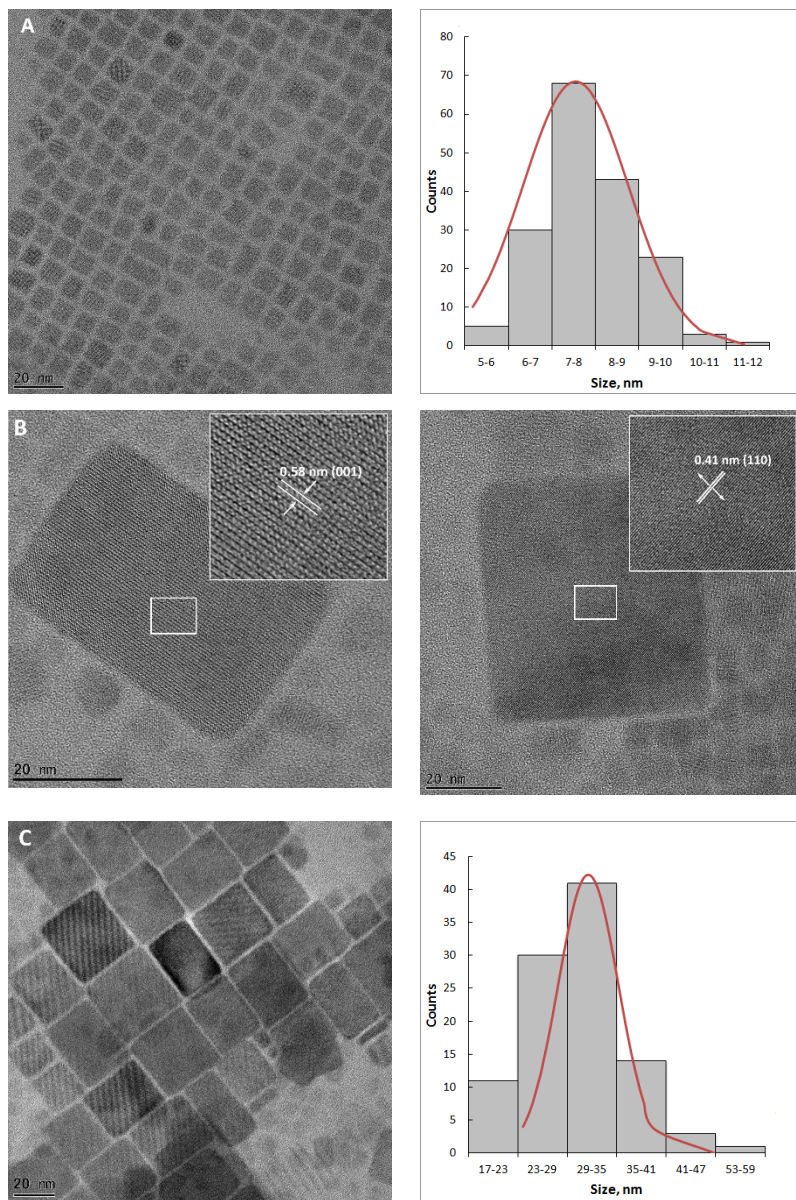


Figure 10. Size evolution of CsPbBr₃ NCs upon DEZ injection. (A) HR TEM image of as-synthesized monodisperse CsPbBr₃ NCs, and size distribution profile; (B) immediate growth of CsPbBr₃ upon DEZ (5wt%) injection. NCs have both orthorhombic and cubic shape. Insets in B: crystal lattice information of grown NCs; (C) HR TEM image of CsPbBr₃ NCs 48 hours after DEZ injection, and size distribution profile.

Interestingly, within 24 hours after DEZ injection, the grown NCs, when in dilute solutions, 'traveled' in distance and self-assembled themselves into highly oriented domains. By approximately 48 hours, the domains grew in size, as more grown NCs attached. Based on the TEM images, we assumed that rectangular shape among grown NCs was observed more often than cubic. High resolution TEM and selected area diffraction (SAED) data demonstrated that grown NCs have cubic crystal phase as well as the original as-synthesized NCs (Figure 11). The Fast Fourier transform (FFT) pattern can be well indexed to be [001] zone axis based on a cubic phase (ICSD 29073). The interplanar distances of the lattice fringes can be measured with $d\{100\}$ and $d\{010\}$, being 5.88 Angstrom.

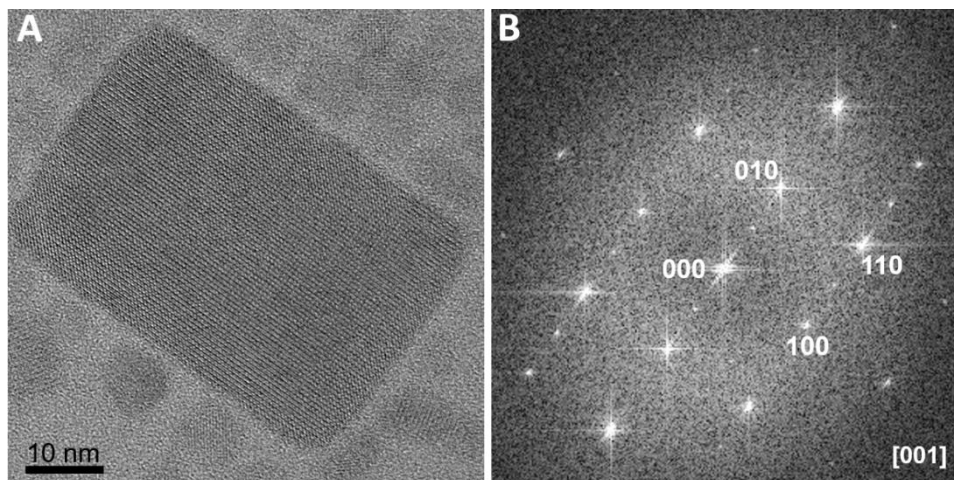


Figure 11. Crystallographic structure of CsPbBr₃ NC after DEZ injection. (A) HR TEM image of CsPbBr₃ nanocrystal; (B) Fast Fourier transform (FFT) pattern of the nanocrystal displayed in A.

It was experimentally found that the injection of DEZ in ratio of 5wt% to as-synthesized NCs produced the best results in terms of their growth and size distribution,

preserving optical and colloidal integrity of NCs. Yet, the excess amount of DEZ lead to NC dissociation within 24h, which resulted in sediment in the form of a yellow powder. It was found that NC size was strongly dependent on the quantity of DEZ added to the NCs. For example, a NC solution with 5 wt. % of DEZ averages 25-35 nm for lateral dimensions, whereas 1 wt. % of DEZ produced NCs of approx. 15 nm. The grown NCs also differ in shape. When 1 wt. % DEZ was used, grown NCs were mostly represented as cubic, whereas 5 wt. % DEZ favored the formation of rectangular NCs (Figure 12).

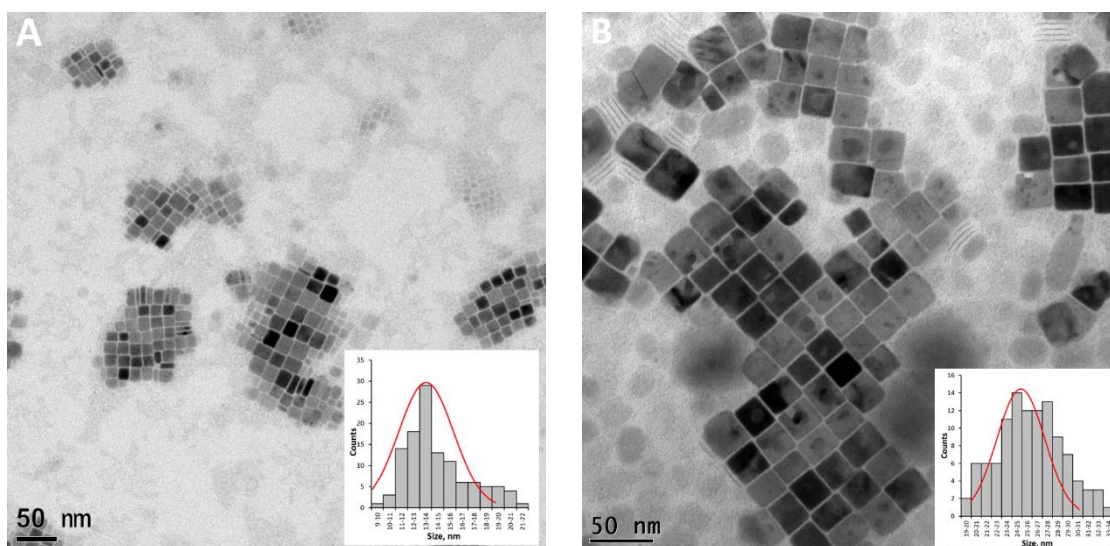
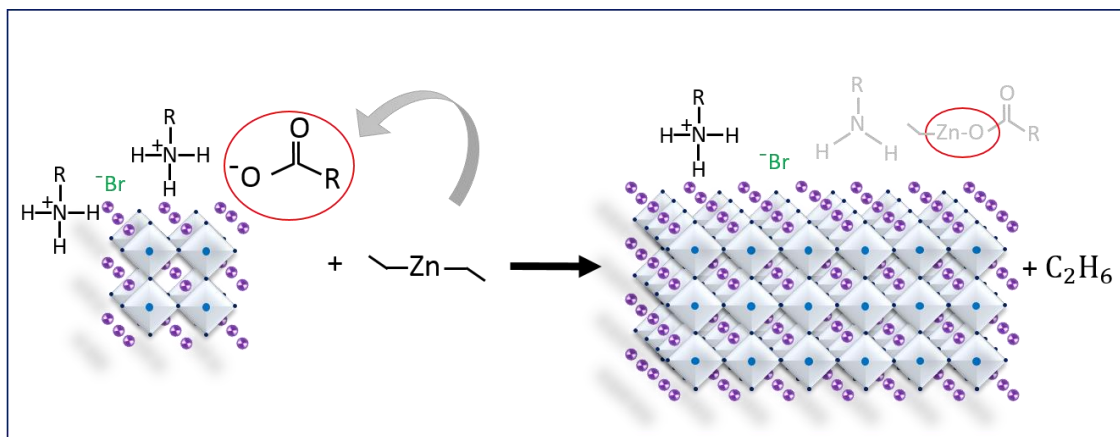


Figure 12. TEM images of CsPbBr₃ NCs after injection of DEZ, and their size distribution profile: (A) CsPbBr₃ NCs with 1 wt. % of DEZ; (B) CsPbBr₃ NCs with 5 wt. % of DEZ.

We postulated that DEZ vigorously reacted with the carboxylate ions on the surface of NCs, forming Zn-O bond, with a subsequent release of ethane as a product of the reaction; oleylammonium donated hydrogen to the remaining ethyl group to form ethane (Scheme 1). Given the exothermic nature of the reaction, and easily destabilizing nature of the dynamic ligands on the surface of NCs, we theorized that the surface reaction lead to an impulsive removal of surfactants and subsequent fusion of NCs, thus resulting in their

bigger size. Of note, the purification of NCs before the addition of DEZ was essential; it allowed the removal of excess of carboxylate anions from the bulk of the colloid, thus shifting the reaction to the surface of the NCs. For the same reason, we also recommend redispersing NCs using anhydrous n-heptane to reduce the amount of moieties present in the solution.



Scheme 1. Proposed reaction path of DEZ with carboxylates on the surface of CsPbBr₃ NCs. Upon dissociation, DEZ reacts with carboxylate anion forming C₂H₅-Zn-OOR compound. Oleylammonium donates hydrogen atom to the remaining ethyl group to produce ethane.

To prove the proposed reaction path, we attempted to detect Zn-O bond by performing Fourier transform infrared spectroscopy (FTIR). Unfortunately, we were not able to detect Zn-O bond, most likely due to its extremely low concentration. Yet, we successfully performed energy dispersive spectroscopy (EDS) for elemental mapping to determine the presence of Zn in NCs after injection. It was found that Zn is mostly concentrated in the areas with grown NCs (Figure 13). This led us to believe that DEZ indeed reacts with carboxylates on the surface of NCs.

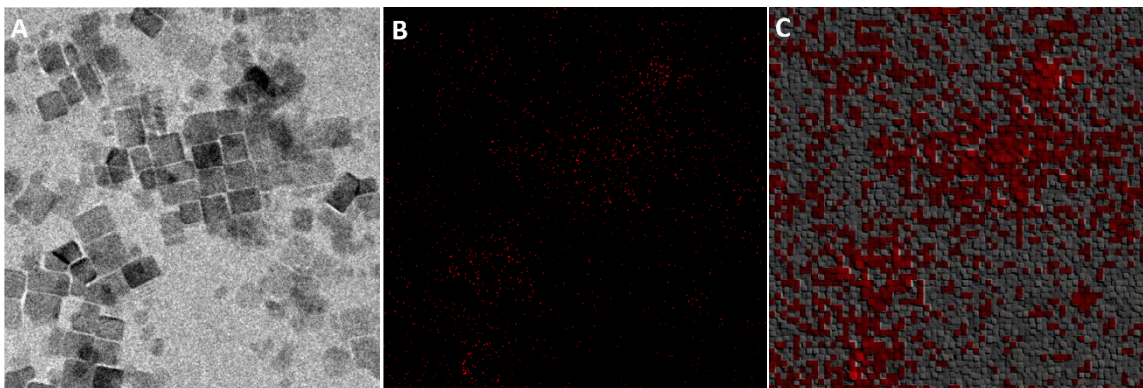


Figure 13. Energy Dispersive Spectroscopy of grown NCs. (A) HR TEM image of a region with grown CsPbBr₃ NCs; (B) Elemental mapping for Zn for a region displayed in (A); (C) Artificially enhanced image of B (red squares represent Zn).

Analysis of grown NCs with TEM revealed a significant increase in lateral dimensions; however, it did not show insight into the thickness of grown NCs. Previous reports on the growth of CsPbBr₃ colloid perovskites at room temperature were mostly associated with two-dimensional nanoplatelets. Consequentially, we were concerned that the injection of DEZ may have led to the actual transformation of as-synthesized NCs to two-dimensional NPLs. To find out whether such transformation occurred, our succeeding work focused on estimating the thickness of grown NCs.

In the effort to determine the thickness of grown NCs, we first studied their optical properties. The obtained data for grown NCs was compared with the as-synthesized NCs. If the proposed theory of NCs growth via induced NC fusion was correct, then we would expect the thickness of modified NCs to be equal to or larger than the thickness of as-synthesized NCs. We would also anticipate a red-shift in their UV-vis and PL spectra, as opposed to the blue shift occurring for 2D NPLs. Our findings: UV-vis spectrum of NCs after DEZ injection displayed a small red shift in the absorption onset (approx. 0.01 eV), and a significant red shift in max absorption peak (approx. 0.12 eV) (Figure 14a). We

concluded that the red shift in the absorption spectra was produced by NCs with smaller band gap values (versus as-synthesized NCs). Despite a significant increase in lateral dimensions of grown NCs, the shift of onset absorption was considerably small. This could be explained by two facts: 1) substantial variability in size distribution among grown NCs after DEZ injection, and/or 2) in contrast to lateral dimensions, NC thickness did not change as appreciably.

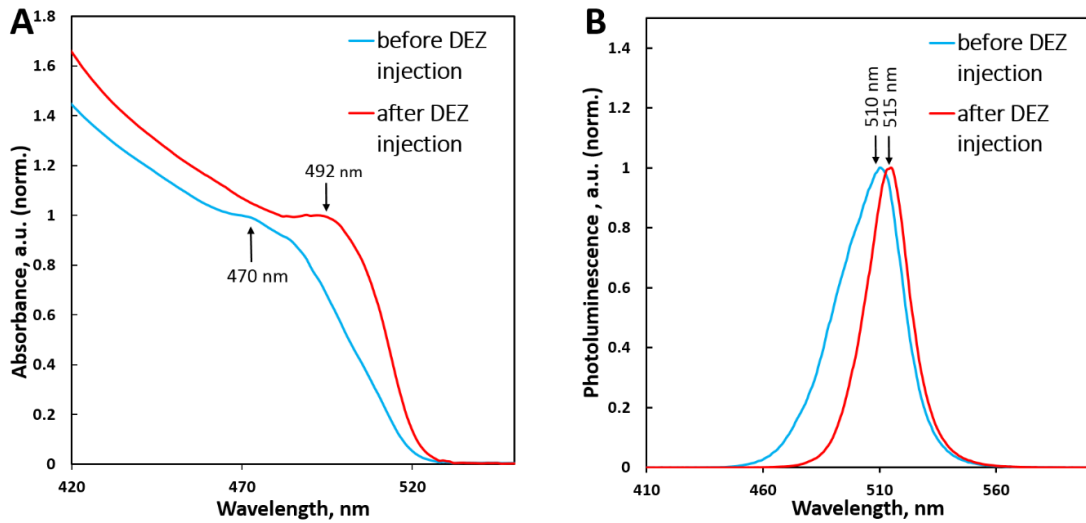


Figure 14. Optical properties of grown NCs. (A) UV-vis absorption and (B) PL emission spectra for CsPbBr₃ before (blue) and after (red) DEZ injection.

We then analyzed PL emission spectrum of modified NCs and again compared it to as-synthesized NCs. As expected, PL spectrum for modified NCs exhibited a red-shifted single peak positioned at 515 nm, in comparison to the exciton peak for as-synthesized NCs at 510 nm (corresponding to 0.02 eV red shift) (Figure 14b). Additionally, we did not observe multiple exciton peaks, which would be characteristic of 2D NPLs with varying thickness [55]. The presence of a single PL peak excluded the formation of 2D NPLs

triggered by DEZ injection, further solidifying our hypothesis of NCs growth via induced fusion.

To provide added confirmation, we produced a 3D model of grown NCs with Electron Tomography (Figure 15). The obtained data revealed that the grown NCs have a relatively uniform thickness of ~ 14 nm. Consequently, the NCs could be confused with NPLs, with regard to their relatively thin rectangular-cuboid shape. In an effort to avoid misleading, we preferred to call them NCs instead of NPLs, implying that they are not two-dimensional structures.

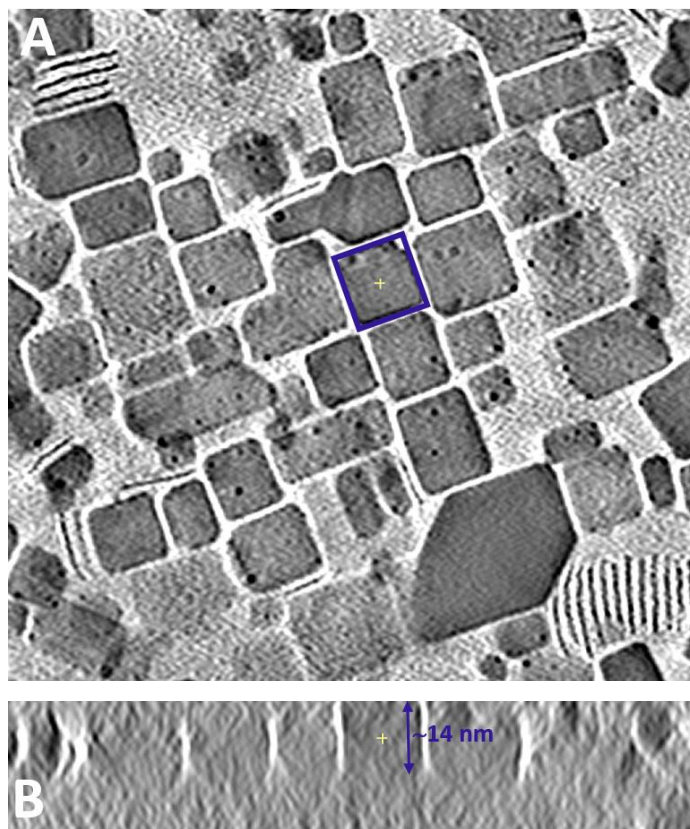


Figure 15. Thickness of grown NCs. (A) Electron Tomography image of CsPbBr₃ NCs after 5wt% DEZ injection; (B) Thickness profile of NC displayed in A.

In the course of this study, we did not attempt to perform a size selective extraction of grown NCs, as the reaction with DEZ significantly reduced the amount of stabilizing ligands (via neutralizing carboxylate and oleylammonium ions on the surface of NCs). Isolation of NCs by centrifugation could be performed only after additional passivation of NCs.

The additional information, including extra HR TEM images, FFT patterns, band gap calculations, and results of the anion-exchange reaction are provided in the Appendix.

Chapter III. CONCLUSIONS AND FUTURE WORK

3.1 Summary and Conclusions

In summary, we discovered a novel chemical route for inducing the growth of as-synthesized CsPbBr₃ perovskite NCs at room temperature. Exothermic chemical reactions, taking place on the surface of NCs, lead to an impulsive removal of highly dynamic surfactants and a subsequent fusion of NCs, resulting in their growth. The performed technique allowed NCs to grow from 8 nm to 35 nm in average lateral dimensions. The thickness was found to be *approx.* 14 nm. It was determined that the growth of NCs happened in all three dimensions, supporting the theory of induced fusion. The growth of NCs resulted in the reduction of their band gaps, producing red shift in both UV-vis absorption and PL spectra of NCs. We believe that the experiments could be effectively expanded to all members of inorganic CsPbX₃ perovskite family.

In conclusion, the discovered chemical route for triggering post-synthetic growth of as-synthesized perovskite NCs offered a new perception on understanding the role of stabilizing surfactants on the NC surfaces. It was shown experimentally that the ligands not only participated in colloidal stabilization and photoluminescence enhancement, but also could be efficiently employed for NC size/band gap and shape manipulations.

3.2 Future Work

Future work will be focused toward narrowing the size distribution of grown NCs, and promoting their utility in photovoltaics. This could be achieved through following steps:

1) Advancing the experiment set up by modifying the system of DEZ injection. In current experiments, DEZ is injected at a single point, and then dispersed in NC solution with the help of a stirring bar. In this type of injection, the NCs tend to grow unevenly (maximum growth happens at a focal point of DEZ injection). Therefore, we are interested in expanding the area of an immediate contact of DEZ with NCs through transforming the tip of the needle itself (injecting DEZ through a few channels simultaneously). Such a transformation should result in narrowing the NC size distribution.

2) Subsequent passivation of grown NCs. The injection of DEZ to NC solution leads to the removal of surfactants. As a result, grown NCs need to be passivated to preserve their colloidal stability and prevent any further agglomeration. Given the ionic nature of perovskite NCs, the new surfactants have to be introduced in the form of ions to allow full surface passivation.

3) Density gradient centrifugation of grown NCs for performing size separation to further examine their optical properties with a focus on size - band gap relations.

4) Thorough analysis of the crystallographic structure of grown NCs with an intent to find out whether the induced fusion of NCs lead to any changes in NC perovskite structure (e.g. doping with Zn^{2+} , vacancies, interstitials, lattice contraction, etc.), and their intrinsic properties (e.g. charge carrier mobility, diffusion length, moisture stability, etc.).

APPENDIX

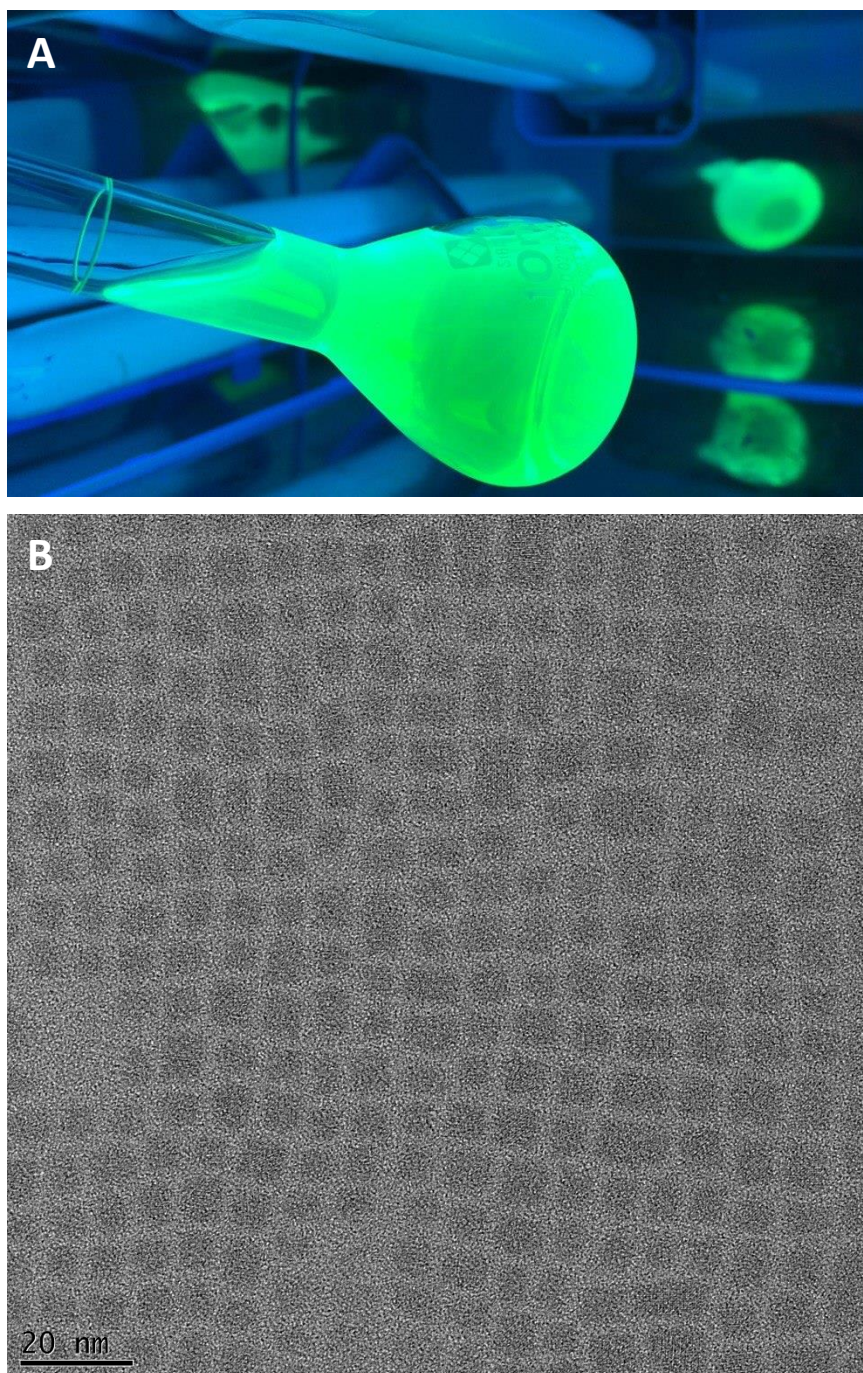


Figure A1. CsPbBr₃ NCs under UV-light (A); HR TEM image of CsPbBr₃ NCs, purified with acetone (B).

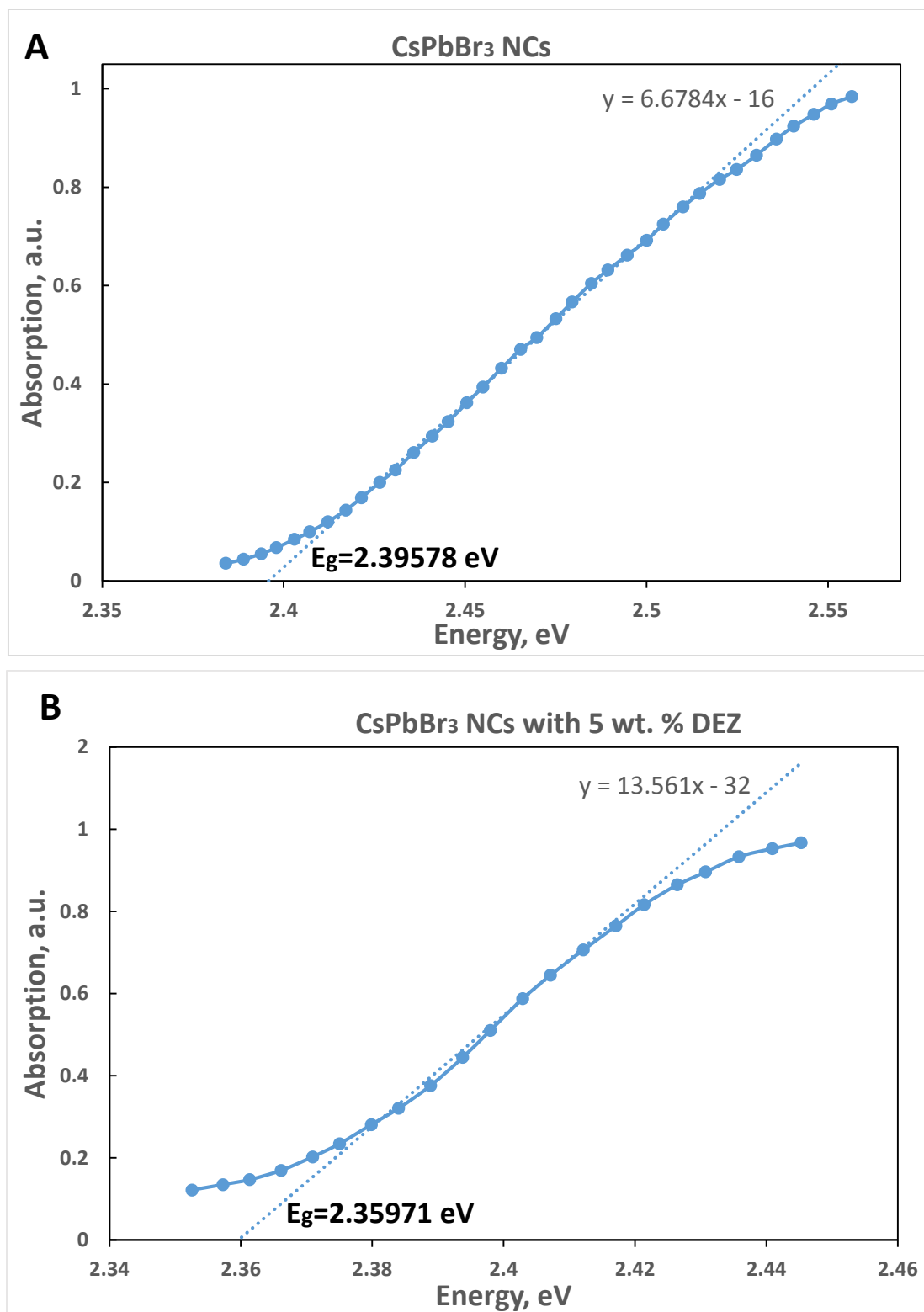


Figure A2. Calculation of band gap from the absorption onset. As-synthesized CsPbBr₃ NCs (A); CsPbBr₃ NCs with 5 wt. % DEZ (B).

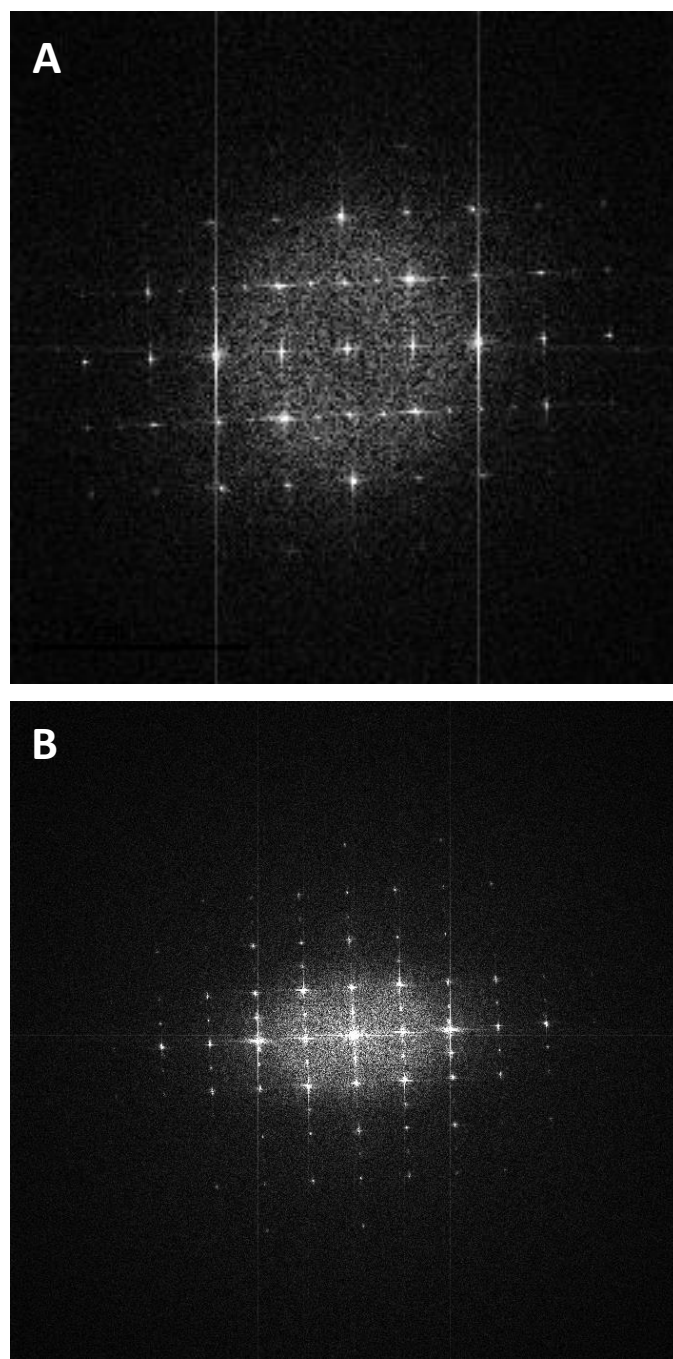


Figure A3. FFT patterns for CsPbBr₃ NCs before (A) and after DEZ injection (B), demonstrating that the cubic perovskite crystallographic structure was preserved after induced NC fusion.

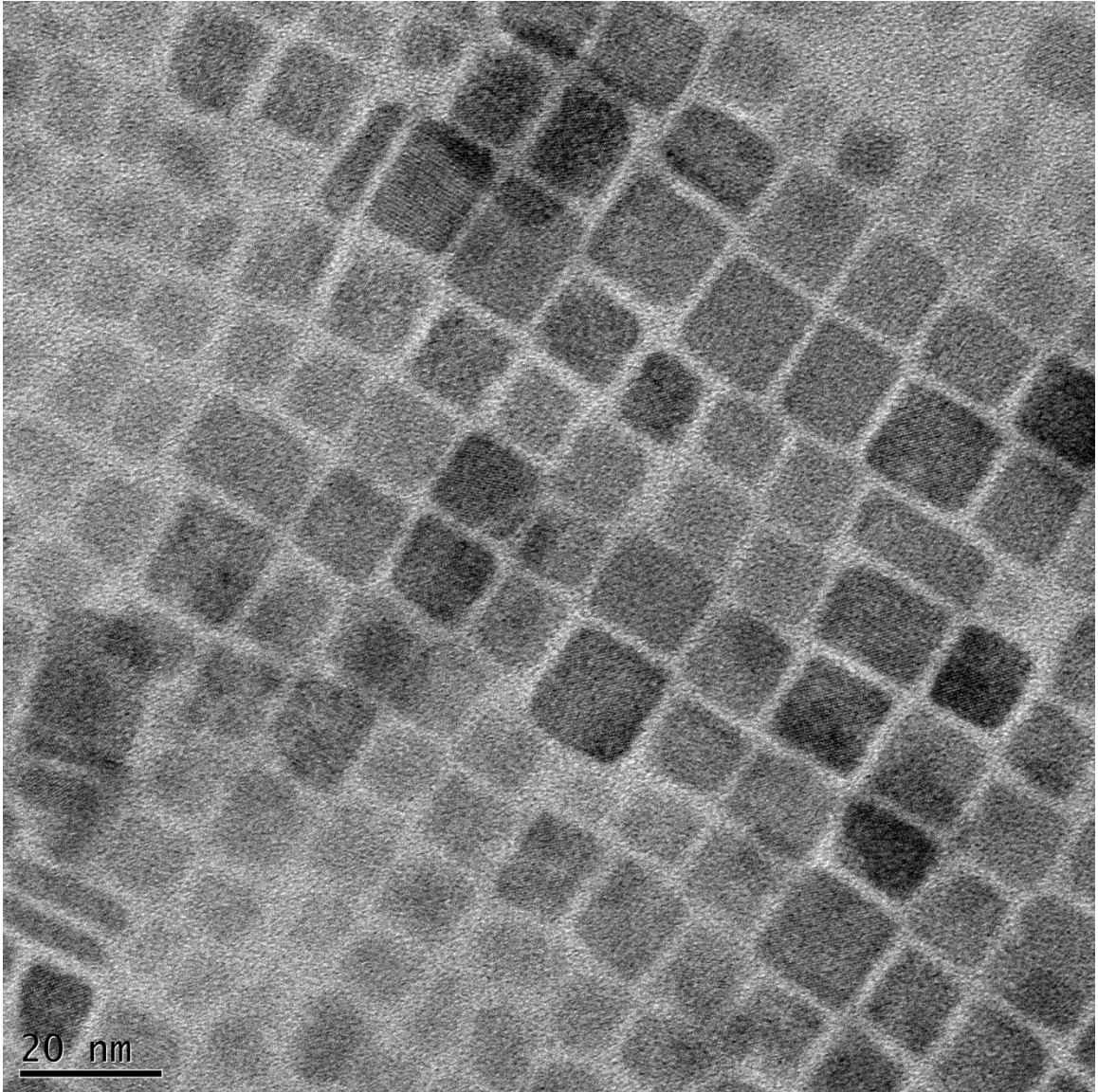


Figure A4. HR TEM image of CsPbBr₃ NCs with 3 wt. % DEZ injection.

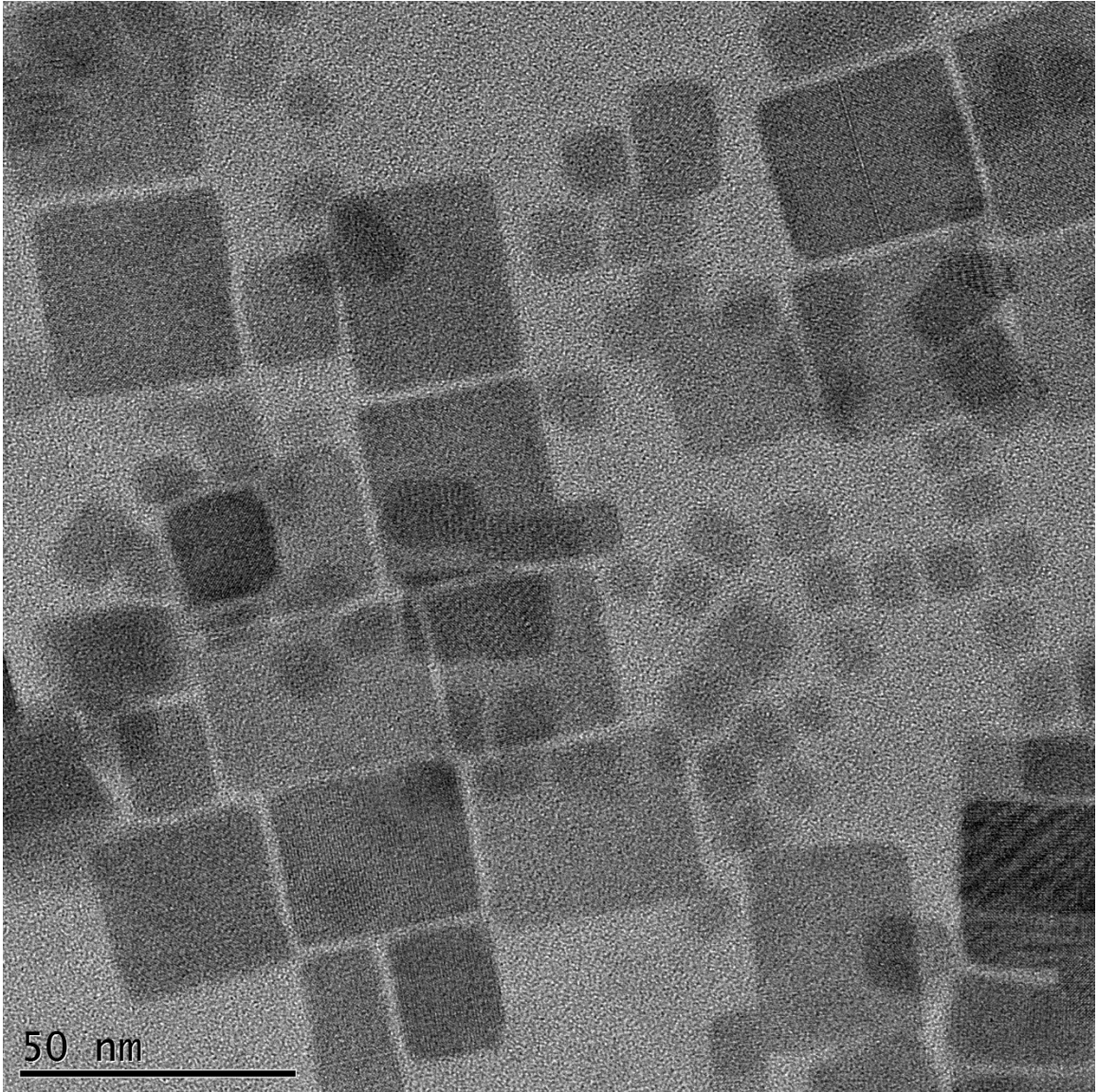


Figure A5. HR TEM image of CsPbBr₃ NCs with **7 wt. %** DEZ.

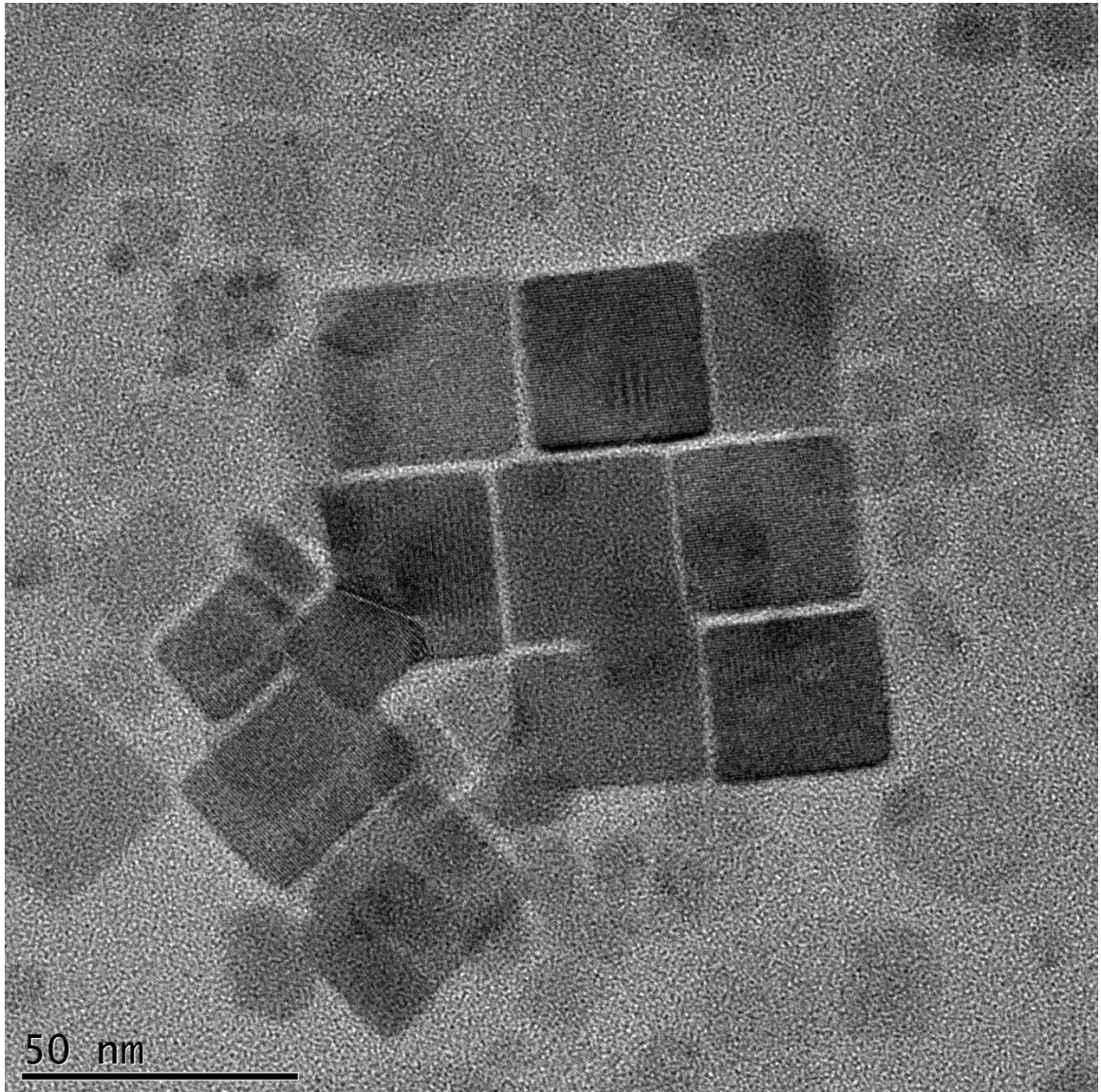


Figure A6. HR TEM image of CsPbBr₃ NCs with **9 wt. %** DEZ.

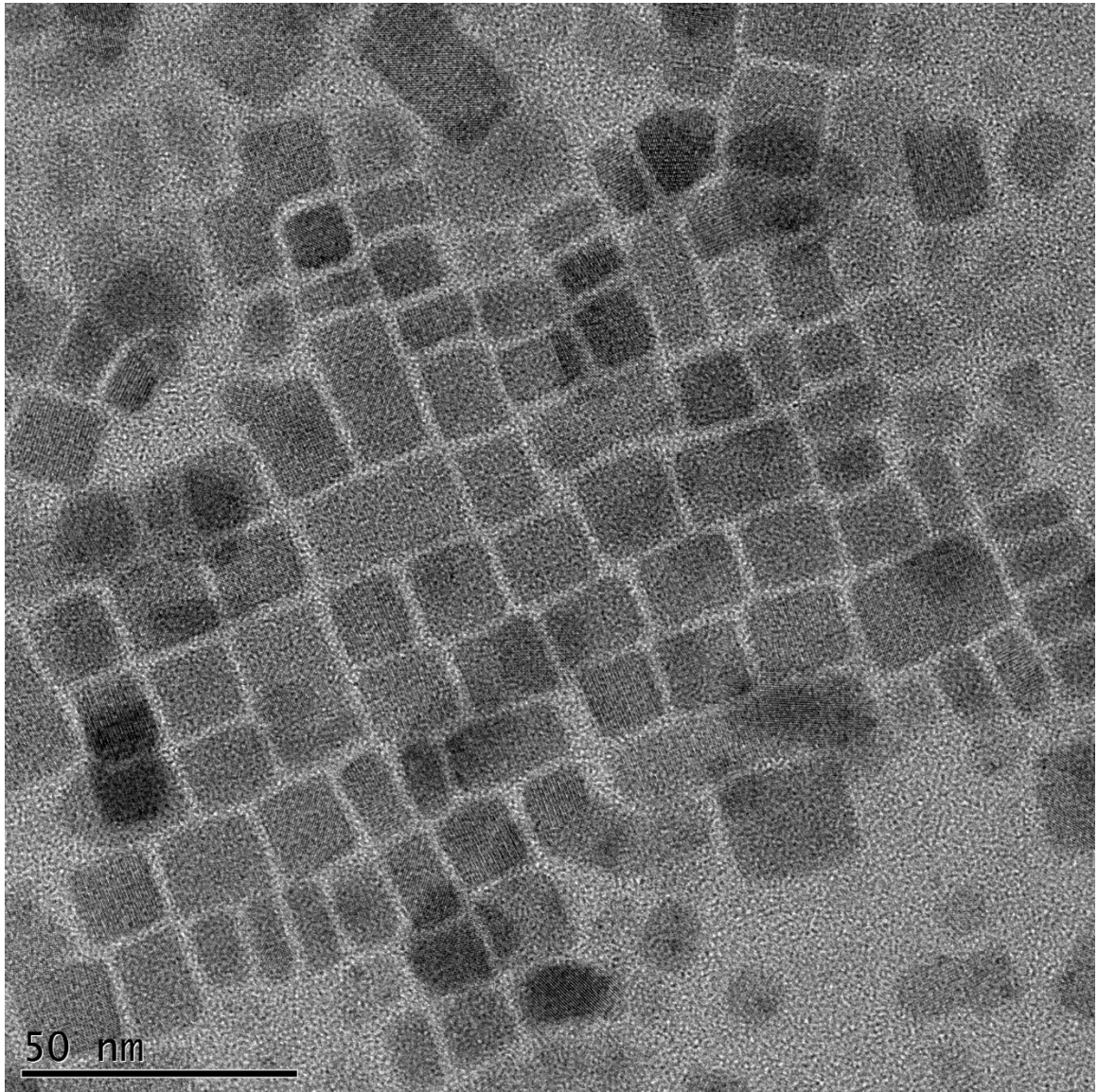


Figure A7. HR TEM image of CsPbBr₃ NCs with **11 wt. %** DEZ.

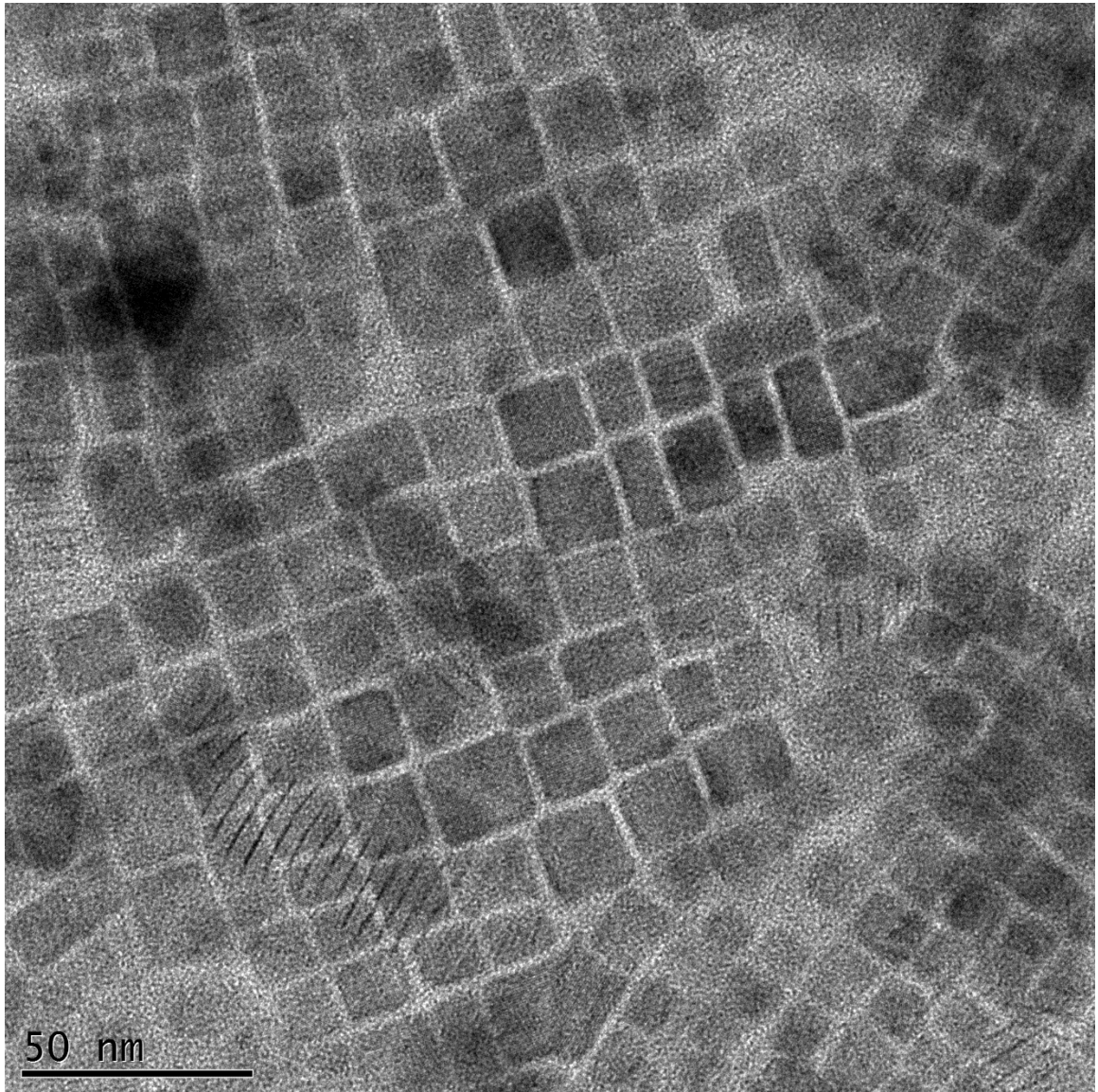


Figure A8. HR TEM image of CsPbBr₃ NCs with **15 wt. %** DEZ injection.

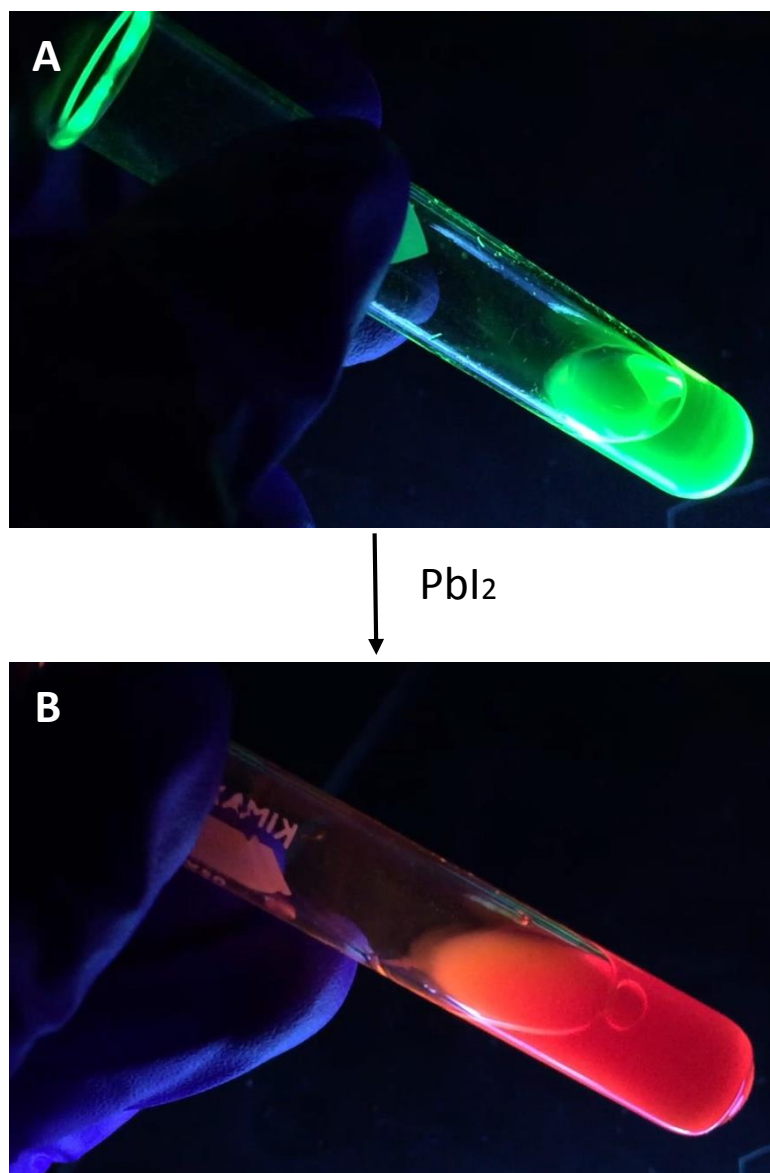


Figure A9. CsPbBr₃ NCs with 5 wt. % DEZ undergoing anion exchange. CsPbBr₃ NCs with 5 wt. % DEZ prior to anion-exchange (A); CsPb(Br/I)₃ NCs as a final product of anion-exchange reaction (B). PbI₂ dissolved in n-heptane with oleic acid and oleylamine was used as a source for I ions. The pictures were taken under UV-light.

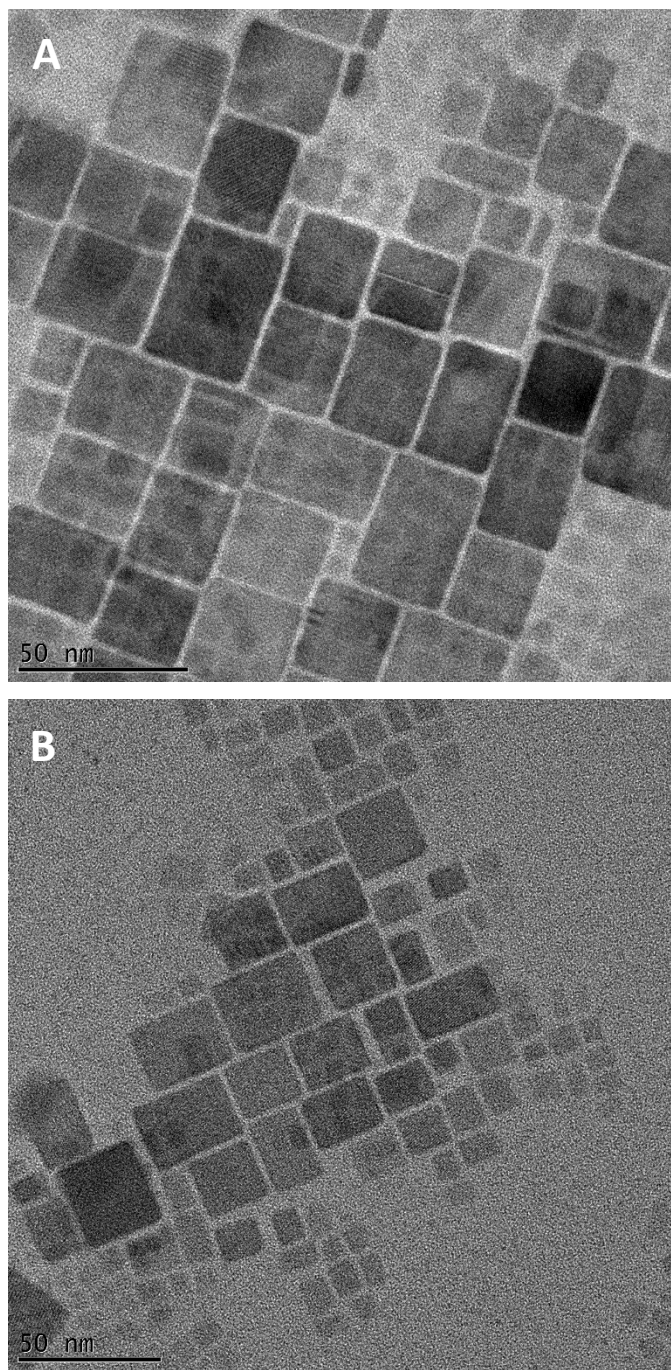


Figure 10A. HR TEM images of CsPbBr₃ NCs with 5 wt. % DEZ prior to anion-exchange (A); CsPb(Br/I)₃ NCs as a final product of anion-exchange reaction (B). PBI₂ was used as a source for I⁻ ions.

BIBLIOGRAPHY

1. Kojima, A.; Teshima, K.; Shirai, Y.; Miyasaka, T. *J. Am. Chem. Soc.* **2009**, 131, 6050.
2. Lee, M. M.; Teuscher, J.; Miyasaka, T.; Murakami, T. N.; Snaith, H. J. *Science* **2012**, 338, 643.
3. Kim, H. S.; Lee, C. R.; Im, J. H.; Lee, K. B.; Moehl, T.; Marchioro, A.; Moon, S. J.; Humphry-Baker, R.; Yum, J. H.; Moser, J. E.; Grätzel, M.; Park, N. G. *Sci. Rep.* **2012**, 2, 591.
4. Yang, W. S.; Noh, J. H.; Jeon, N. J.; Kim, Y. C.; Ryu, S.; Seo, J.; Seok, S. I. *Science* **2015**, 348, 1234.
5. Saliba, M.; Matsui, T.; Seo, J. Y.; Domanski, K.; Correa-Baena, J. P.; Nazeeruddin, M. K.; Zakeeruddin, S. M.; Tress, W.; Abate, A.; Hagfeldt, A.; Gratzel, M. *Energy Environ Sci.* **2016**, 9, 1989.
6. Ergen, O.; Gilbert, S. M.; Pham, T.; Turner, S. J.; Tan, M. T. Z.; Worsley, M. A.; Zettl, A. *Nat. Mater.* **2017**, 16, 522.
7. Kulbak, M.; Cahen, D.; Hodes, G. *J. Phys. Chem. Lett.* **2015**, 6, 2452.
8. Protesescu, L.; Yakunin, S.; Bodnarchuk, M. I.; Krieg, F.; Caputo, R.; Hendon, C. H.; Yang, R.; Walsh, A.; Kovalenko, M. V. *Nano Lett.* **2015**, 6, 3692.
9. Sun, S.; Yuan, D.; Xu, Y.; Wang, A.; Deng, Z. *ACS Nano* **2016**, 10, 3648.
10. Li, X.; Wu, Y.; Zhang, S.; Cai, B.; Gu, Y.; Song, J.; Zheng, H. *Adv. Funct. Mater.* **2016**, 26, 2435.
11. Wang, Y.; Sun, X.; Shivanna, R.; Yang, Y.; Chen, Z.; Guo, Y.; Wang, G. G.; Wertz, E.; Deschler, F.; Cai, Z.; Zhou, H.; Lu, T. M.; Shi, J. *Nano Lett.* **2016**, 16, 7974.
12. Chen, J.; Fu, Y.; Samad, L.; Dang, L.; Zhao, Y.; Shen, S.; Guo, L.; Jin, S. *Nano Lett.* **2017**, 17, 460.
13. De Roo, J.; Ibáñez, M.; Geiregat, P.; Nedelcu, G.; Walravens, W.; Maes, J.; Martins, J. C.; Van Driessche, I.; Kovalenko, M. V.; Hens, Z. *ACS Nano*, **2016**, 10, 2071.

14. Wei, S.; Yang, Y.; Kang, X.; Wang, L.; Huang, L.; Pan, D. *Chem. Commun.* **2016**, 52, 7265.
15. Bekenstein, Y.; Koscher, B. A.; Eaton, S. W.; Yang, P.; Alivisatos, A. P. *J. Am. Chem. Soc.* **2015**, 137, 16008.
16. Akkerman, Q. A.; Motti, S. G.; Kandada, A. R. S.; Mosconi, E.; D'Innocenzo, V.; Bertoni, G.; Marras, S.; Kamino, B. A.; Miranda, L.; De Angelis, F.; Petrozza, A.; Prato, M.; Manna, L. *J. Am. Chem. Soc.*, **2016**, 138, 1010.
17. Nedelcu, G.; Protesescu, L.; Yakunin, S.; Bodnarchuk, M. I.; Grotevent, M. J.; Kovalenko, M. V. *Nano Lett.* **2015**, 15, 5635.
18. Pan, A.; He, B.; Fan, X.; Li, Z.; Urban, J. J.; Alivisatos, A. P.; He, L.; Liu, Y. *ACS Nano*, **2016**, 10, 7943.
19. Yin, W. J.; Shi, T.; Yan, Y. *Adv. Mater.* **2014**, 26, 4653.
20. Stoumpos, C. C.; Malliakas, C. D.; Peters, J. A.; Liu, Z.; Sebastian, M.; Im, J.; Chasapis, T. C.; Wibowo, A. C.; Chung, D. Y.; Freeman, A. J.; Wessels, B. W.; Kanatzidis, M. G. *Cryst. Growth Des.* **2013**, 13, 2722.
21. Jacoboni, C.; Canali, C.; Ottaviani, G.; Quaranta, A. A. *Solid State Electron.* **1977**, 20, 77.
22. Stranks, S. D.; Eperon, G. E.; Grancini, G.; Menelaou, C.; Marcelo J. P. Alcocer; Leijtens, T.; Herz, L. M.; Petrozza, A.; Snaith, H. J. *Science* **2013**, 342, 341.
23. Xing, G.; Mathews, N.; Sun, S.; Lim, S. S.; Lam, Y. M.; Grätzel, M.; Mhaisalkar, S.; Sum, T. C. *Science* **2013**, 342, 344.
24. Du, M. H. *J. Mater. Chem. A* **2014**, 2, 9091.
25. Green, M. A.; Ho-Baillie, A.; Snaith, H. J. *Nat. Photonics* **2014**, 8, 506.
26. Zuo, C.; Bolink, H. J.; Han, H.; Huang, J.; Cahen, D.; Ding, L. *Adv. Sci.* **2016**, 3, 1500324.
27. Tang, H.; He, S.; Peng, C. *Nanoscale Res Lett.* **2017**, 12, 410.

28. National Renewable Energy Laboratory, Best Research-Cell Efficiencies Chart. <https://www.nrel.gov/pv/assets/images/efficiency-chart.png> (accessed October 2017).
29. Lee, J. W.; Kim, D. H.; Kim, H. S.; Seo, S. W.; Cho, S. M.; Park, N. G. *Adv. Energy Mater.* **2015**, *5*, 1501310.
30. Saliba, M.; Matsui, T.; Seo, J. Y.; Domanski, K.; Correa-Baena, J. P.; Nazeeruddin, M. K.; Zakeeruddin, S. M.; Tress, W.; Abate, A.; Hagfeldt, A.; Grätzel, M. *Energy Environ. Sci.* **2016**, *9*, 1989.
31. McMeekin, D. P.; Sadoughi, G.; Rehman, W.; Eperon, G. E.; Saliba, M.; Hörantner, M. T.; Haghighirad, A.; Sakai, N.; Korte, L.; Rech, B.; Johnston, M. B.; Herz, L. M.; Snaith, H. J. *Science* **2016**, *351*, 151.
32. Eperon, G. E.; Paternò, G. M.; Sutton, R. J.; Zampetti, A.; Haghighirad, A. A.; Cacialli, F.; Snaith, H. J. *J. Mater. Chem. A* **2015**, *3*, 19688.
33. Luo, P.; Xia, W.; Zhou, S.; Sun, L.; Cheng, J.; Xu, C.; Lu, Y. *J. Phys. Chem. Lett.* **2016**, *7*, 3603.
34. Swarnkar, A.; Marshall, A. R.; Sanhira, E. M.; Chernomordik, B. D.; Moore, D. T.; Christians, J. A.; Chakrabarti, T.; Luther, J. M. *Science* **2016**, *354*, 92.
35. Liang, J.; Wang, C.; Wang, Y.; Xu, Z.; Lu, Z.; Ma, Y.; Zhu, H.; Hu, Y.; Xiao, C.; Yi, X.; Zhu, G.; Lv, H.; Ma, L.; Chen, T.; Tie, Z.; Jin, Z.; Liu, J. *J. Am. Chem. Soc.* **2016**, *138*, 15829.
36. Chang, X.; Li, W.; Zhu, L.; Liu, H.; Geng, H.; Xiang, S.; Liu, J.; Chen, H. *ACS Appl. Mater. Interfaces* **2016**, *8*, 33649.
37. Ye, S.; Xiao, F.; Pan, X. Y.; Ma, Y. Y.; Zhang, Q. Y. *Mater. Sci. Eng. R* **2010**, *71*, 1.
38. Song, J.; Li, J.; Li, X.; Xu, L.; Dong, Y.; Zeng, H. *Adv. Mater.* **2015**, *27*, 7162.
39. Pan, J.; Quan, L. N.; Zhao, Y.; Peng, W.; Murali, B.; Sarmah, S. P.; Yuan, M.; Sinatra, L.; Alyami, N. M.; Liu, J.; Yassitepe, E.; Yang, Z.; Voznyy, O.; Comin, R.; Hedhili, M. N.; Mohammed, O. F.; Lu, Z. H.; Kim, D. H.; Sargent, E. H.; Bakr, O. M. *Adv. Mater.* **2016**, *26*, 4595.
40. Ramasamy, P.; Lim, D. H.; Kim, B.; Lee, S. H.; Lee, M. S.; Lee, J. S. *Chem. Commun.*, **2016**, *52*, 2067.

41. Song, J.; Xu, L.; Li, J.; Xue, J.; Dong, Y.; Li, X.; Zeng, H. *Adv. Mater.*, **2016**, 28, 4861.
42. Bekenstein, Y.; Koscher, B. A.; Eaton, S. W.; Yang, P.; Alivisatos, A. P. *J. Am. Chem. Soc.* **2015**, 137, 16008.
43. Udayabhaskararao, T.; Kazes, M.; Houben, L.; Lin, H.; Oron, D. *Chem. Mater.*, **2017**, 29, 1302.
44. Kim, Y.; Yassitepe, E.; Voznyy, O.; Comin, R.; Walters, G.; Gong, X.; Kanjanaboos, P.; Nogueira, A. F.; Sargent, E. H. *ACS Appl. Mater. Interfaces*, **2015**, 7, 25007.
45. De Roo, J.; Ibáñez, M.; Geiregat, P.; Nedelcu, G.; Walravens, W.; Maes, J.; Martins, J. C.; Van Driessche, I.; Kovalenko, M. V.; Hens, Z. *ACS Nano*, **2016**, 10, 2071.
46. Roth, A. P.; Williams, D. F. *J. Appl. Phys.*, **1981**, 52, 6685.
47. Oda, S.; Tokunaga, H.; Kitajima, N.; Hanna, J.-I.; Shimizu, I.; Kokado, H. *Jpn. J. Appl. Phys.*, **1985**, 24, 1607.
48. Hu, J.; Gordon, R. G. *Solar Cells*, **1991**, 30, 437.
49. Hu, J.; Gordon R. G. *J. Appl. Phys.*, **1992**, 71, 880.
50. Hu, J.; Gordon R. G. *J. Appl. Phys.*, **1992**, 72, 5381.
51. Kim, Y. S.; Won, Y. S. *Bull. Korean Chem. Soc.*, **2009**, 30, 1573.
52. Weckman, T.; Laasonen, K. *J. Phys. Chem. C.*, **2016**, 120, 21460.
53. Hudson, A. R. *Phys. Rev. Lett.*, **1960**, 4, 505.
54. Ghandhi, S. K.; Field, R. J.; Shealy, J. R. *Appl. Phys. Lett.*, **1980**, 37, 449.
55. Tyagi, P.; Arveson, S. M.; Tisdale, W. A. *J. Phys. Chem. Lett.*, **2015**, 6, 1911.
56. Chen, O.; Zhao, J.; Chauhan, V. P.; Cui, J.; Wong, C.; Harris, D. K.; Wei, H.; Han, H.-S.; Fukumura, D.; Jain, R. K.; Bawendi, M. G. *Nat. Mater.* **2013**, 12, 445.

57. Christodoulou, S.; Vaccaro, G.; Pinchetti, V.; De Donato, F.; Grim, J. Q.; Casu, A.; Genovese, A.; Vicidomini, G.; Diaspro, A.; Brovelli, S.; Manna, L.; Moreels, I. *J. Mater. Chem. C* **2014**, *2*, 3439.